~~Intertidal spring discharge to a coastal ecosystem and impacts of climate change on future groundwater temperature~~Present and future thermal regimes of intertidal groundwater springs in a threatened coastal ecosystem~~: A multi-method investigation~~

Jason J. KarisAllen[1], Aaron A. Mohammed[1,2], Joseph J. Tamborski[3], Rob C. Jamieson[1], Serban Danielescu[4,5], Barret L. Kurylyk[1]

[1]Department of Civil and Resource Engineering and Centre for Water Resources Studies, Dalhousie University, Halifax, B3H 4R2, Canada
[2]Department of Earth and Planetary Sciences, McGill University, Montreal, H3A 0E8, Canada
[3]Department of Ocean and Earth Sciences, Old Dominion University, Norfolk, VA, 23529, USA
[4]Water Science and Technology Directorate, Environment and Climate Change Canada, Burlington, ON L7S 1A1, Canada
[5]Agriculture and Agri-Food Canada, Fredericton Research and Development Centre, Fredericton, New Brunswick E3B 4Z7, Canada

Correspondence to: Barret L. Kurylyk (barret.kurylyk@dal.ca)

Abstract

In inland settings, groundwater discharge ~~is known to~~ thermally modulates receiving surface water bodies and provides localized thermal refuges; however, the thermal influence of intertidal springs on coastal waters and their thermal sensitivity ~~of these springs~~ to climate change are not well studied. We paired ~~*in-situ* thermal and hydrologic monitoring with~~ analyses of drone-based thermal imagery with *in-situ* thermal and hydrologic monitoring to estimate ~~the~~ discharge to the lagoon from intertidal springs and groundwater-dominated streams in summer 2020. Results, which were generally supported by independent radon-based groundwater discharge estimates, revealed that ~~the~~ combined summertime spring inflows (0.047 m^3 s^{-1}) were comparable to ~~the~~ combined stream inflows (0.050 m^3 s^{-1}). ~~Heat flux analyses indicated that the~~NI ~~n~~Net advection for the streams and springs were also comparable to each other but were two orders of magnitude less than the downwelling shortwave radiation across the lagoon. Although ~~the~~ lagoon-scale thermal effects of groundwater inflows were small compared to atmospheric forcing, spring discharge dominated heat transfer at a local scale, creating pronounced cold-water plumes along the shoreline.

A numerical model was used to interpret measured groundwater temperature data and investigate seasonal and multi-decadal groundwater temperature patterns. Modelled seasonal temperatures were used to relate measured spring temperatures to their respective aquifer source depths, ~~and~~ while multi-decadal simulations forced by historic and projected climate data were used to assess ~~to consider~~ long-term groundwater warming. Based on the ~~different~~ 2020-2100 climate scenarios ~~used for 2020 to~~

~~2100~~ (for which 5-year averaged air temperature increased up to 4.32°C), modelled 5-year averaged subsurface temperatures increased 0.08-~~ to ~~2.23°C in shallow groundwater (4.2 m depth) and 0.32~~ to~~- 1.42°C in the deeper portion of the aquifer (13.9 m), indicating the depth-dependency of warming. This study presents the first analysis of the thermal sensitivity of groundwater-dependent coastal ecosystems to climate change and indicates that coastal ecosystem management should consider ~~the~~ potential impacts of groundwater warming.

1 Introduction

Global freshwater temperatures have been increasing in response to changes to climate and landcover (Desbruyères et al., 2017; IPCC, 2014; Isaak et al., 2017; Liu et al., 2020). Water temperature is a critical consideration in aquatic ecophysiology, as it influences the metabolic functions of all organisms (e.g., Morash et al., 2021) and the biogeochemistry of aquatic systems (Ouellet et al., 2020). Cold-water patches, sourced by discrete groundwater inflows to streams, form thermal refuges that enable heat-sensitive species to survive periods of elevated thermal stress (Kurylyk et al., 2015a; Sullivan et al., 2021; Torgersen et al., 2012; Wilbur et al., 2020). This cooling mechanism depends on the seasonal stability of groundwater temperature relative to surface water due to the insulative effect of ground overlying the source groundwater (Bonan, 2008). In addition to stable temperatures, focused groundwater discharge ~~points~~ locations in surface water bodies are often characterised by distinct biogeochemical conditions preferred by certain aquatic species (Cantonati et al., 2020; Hayashi & Rosenberry, 2002). Although groundwater-dependent ecosystems may be more resilient to seasonal and short-term ~~extreme~~ weather changes, they remain susceptible to multi-decadal warming signals that can penetrate deeper into the subsurface to affect groundwater temperatures (Bense & Kurylyk, 2017; Gunawardhana & Kazama, 2011; Menberg et al., 2014; Benz et al., 2022).

Surface water temperatures in inland lotic systems are influenced by latent, sensible, and radiative heat fluxes at the water surface, longitudinal heat flux along the channel due to advection and dispersion, and bed heat fluxes due to friction, conduction, and advection (Caissie, 2006; Dugdale et al., 2017), which in turn are controlled by landscape characteristics (O'Sullivan et al., 2019). The thermal regimes of many coastal aquatic systems are inherently more complex than freshwater systems as they are additionally influenced by exchanges with the ocean (e.g., Newton & Mudge, 2003). Furthermore, vertical and horizontal thermal stratification within coastal waters may arise due to salinity-induced density differences (e.g., Danielescu et al., 2009; Newton & Mudge, 2003; Nunes & Lennon, 1987). These complex thermal processes and patterns may contribute to the relative lack of study of ~~the thermal regimes of estuaries and lagoons~~coastal thermal regimes compared to inland lotic waters. ~~Nevertheless~~However, a few studies have shown that net solar radiation, latent heat of evaporation, and sensible heat transfer to the atmosphere are typically ~~remain~~ the primary thermal drivers in shallow coastal waters (e.g., Ji, 2017; Rodríguez-Rodríguez & Moreno-Ostos, 2006).

Despite the large body of recent work and associated reviews characterising river (Caissie, 2006; Dugdale et al., 2017; Ouellet et al., 2020), ocean (Abraham et al., 2013), and subsurface thermal regimes (Kurylyk et al., 2014a), relatively little work has focused on the influence of groundwater on the temperature of transitional coastal waters (e.g., Chikita et al., 2015; Rodríguez-Rodríguez & Moreno-Ostos, 2006). Groundwater may be delivered to the coast via direct (e.g., springs) and indirect (i.e., baseflow in streams or rivers) pathways and can influence coastal ecosystems (Luijendijk et al., 2020). As is the case for rivers, groundwater inputs to coastal environments may generate spatial thermal heterogeneity in the receiving water body (e.g., Danielescu et al., 2009; KarisAllen & Kurylyk, 2021), but the ability of these cold-water plumes to serve as thermal refuges is less explored. Further, although some riverine studies have considered the sensitivity of incoming groundwater to future climate change (e.g., Hannah & Garner, 2015; Kaandorp et al., 2019; Kurylyk et al., 2014b), to our knowledge no studies have investigated the thermal sensitivity of coastal groundwater discharge to climate change or the potential ecological consequences. Thermal sensitivity is broadly used in hydrology to refer to the change in water temperature due to atmospheric forcing (e.g., Kelleher et al., 2012). In the present context, thermal sensitivity refers to the change in groundwater temperature in response to climate change, which can be quantified as the ratio of the change in mean annual groundwater temperature to the change in mean annual air temperature (Kurylyk et al., 2015b).

Thermal imaging devices attached to aircraft have been used to aerially map thermal heterogeneity in coastal zones resulting from direct groundwater input (e.g., Coluccio et al., 2020; Danielescu et al., 2009; Lee et al., 2016a). Previous studies have utilized thermal infrared imagery to estimate local groundwater discharge via empirical relationships with thermal plume geometry (e.g., Bejannin et al., 2017; Danielescu et al., 2009; Kang et al., 2019; Kelly et al., 2019b; Lee et al., 2016a; Mundy et al., 2017; Tamborski et al., 2015). Small rotary-wing drones have the capacity to inexpensively collect thermal data with higher temporal and spatial resolution relative to conventional occupied aircraft (Dugdale et al., 2022; Lee et al., 2016b), although drone thermal data often involve additional challenges (e.g., thermal drift and limited spatial coverage; Dugdale et al., 2019; Kelly et al., 2019a). Despite these issues, this technology is suitable for determining relative temperature differences in individual images and thus can be used to locate focused groundwater inputs that generate anomalous water temperatures.

~~The overall goals of this study~~Knowledge gaps related to the hydrologic and thermal functioning of inter-tidal springs in coastal ecosystems and their thermal sensitivity to climate change provided the impetus for the present study. Our goals were to (1) quantify the discharge and present thermal influence of inter-tidal springs in a warm coastal lagoon ecosystem and (2) investigate how these springs will be thermally impacted by climate change using a numerical model informed by field data. Field and modeling work was conducted for a Marine Protected Area in eastern Canada with relatively high water temperatures (up to 33°C) and a thermally stressed ~~unique~~ ecosystem with an endemic strain of Irish moss. Drone thermal imaging was paired with *in-situ* thermal and hydrologic monitoring to locate and further investigate spring and groundwater-dominated stream inputs to the lagoon. ~~Comparison to stream inputs was conducted to emphasize the relative importance of focused intertidal springgroundwater discharge at this site.~~ ~~Spring discharge estimated via drone thermal imagery and flow gauging~~

~~was compared with total direct groundwater input estimated by using radon as a groundwater tracer.~~ To interpret our measured spring temperatures and better understand how the aquifer and consequently the springs will respond to future warming, a numerical heat transfer model calibrated with groundwater data was applied to relate measured seasonal temperature signals at springs to their respective aquifer source depths and to simulate depth-dependent aquifer warming due to climate change ~~between 2020 and 2100~~. Field data and numerical modeling results were collectively used to assess our hypothesis that springs within this lagoon will be sourced from different depths and thus that some springs will manifest thermal impacts of climate change more quickly than others.

2 Site description

The study took place in the Basin Head lagoon on the eastern shore of Prince Edward Island (PEI) in Atlantic Canada (Fig. 1). The lagoon was established as a Marine Protected Area in 2005 under the *Oceans Act* to protect giant Irish moss, a unique morphotype of Irish moss (*Chondrus crispus*) endemic to the lagoon (DFO, 2009). The biomass of giant Irish moss within the lagoon declined by over 99% from 1980 to 2008 (DFO, 2009), and thermal stress has been identified as one of the compounding stressors contributing to its decline (Joseph et al., 2021). ~~The~~ Basin Head lagoon is approximately 0.6 km^2, with water depths that rarely exceed 2 m at high tide. The lagoon has a mixed semi-diurnal tide, with an average range of approximately 0.8 m, and is connected to the ocean by a narrow, artificial channel (Fig. 1b).

PEI is characterized by mean annual precipitation ranging from 1046 to 1241 mm yr^{-1} and mean monthly air temperatures from -7.9 to 18.6°C based on historical records of eight Environment and Climate Change Canada (ECCC) weather stations (Rivera, 2014). Precipitation is routed from the Basin Head watershed to the lagoon via groundwater-dominated streams (Fig. 1b) and direct groundwater discharge pathways. PEI bedrock aquifers are typically weakly consolidated, very fine to coarse, fractured sandstones with sparse occurrences of mudstone, conglomerate, and/or breccia (Brandon, 1966; Crowl, 1969a; van de Poll, 1989). Surficial tills within the study watershed are mainly clay-sand to sand phase tills (Crowl, 1969b; Prest, 1973) and are estimated to be 5 m deep on average based on local core logs (Government of PEI, 2019).

3 Methods

Several methods were collectively used to test our primary hypothesis and undertake our objectives~~,~~ (Fig. 2). These are described in the following sections but are briefly summarized here to elucidate their interrelationships. Thermal-based drone mapping and analysis were used to identify spring locations and delineate the size of their thermal plumes (box 1, Fig. 2). Selected springs, streams, and a coastal piezometer (~~locations in~~ Fig. 1) were instrumented for *in-situ* thermal and level monitoring (box 2). Thermal plume sizes (box 1) and flows (box 2) for selected springs underpinned an empirical relationship between plume area and spring discharge (box 3), which was applied to all springs to estimate total spring discharge to the lagoon (output 1). This total spring discharge was compared to total groundwater (springs plus non-point source diffusive flow) discharge estimates from a radon mass balance ~~-~~(box 4). The groundwater discharge estimates from thermal imagery were also used~~the~~ to estimate heat advection at the lagoon scale for the springs and streams (output 1) to assess their ecosystem impacts. Temperature data from a piezometer and well (box 2) were used in concert with climate data (box 5) to calibrate and drive a numerical model of groundwater temperature (box 6) for present and future climate conditions. Depth-dependent seasonal temperature signals in the calibrated model were compared to measured spring temperatures (box 2) to estimate the aquifer depths feeding those springs. Finally, simulated future groundwater temperatures (box 6) were used to provide insight into how springs sourced from different depths may warm in the future (output 2).

Field work and data collection~~, including the instrumentation of springs and streams and the installation of a climate station and coastal piezometer (Fig. 1b),~~ for this study occurred between June 2019 and November 2020. Lagoon water temperatures typically peak in July and August in the Basin Head lagoon, which reflects the period of greatest thermal stress for giant Irish moss. Contrast between groundwater and lagoon water temperatures is also greatest in July and August, which is favourable for the detection of springs via thermal infrared imaging. Accordingly, a dense network of sensors (Fig. 1) was temporarily installed between July 23 and August 26, 2020, to provide a more detailed assessment of groundwater discharge (i.e., the 35-day 'focused study period') during this critical period. Drone thermal images were captured in the summer of 2020, and radon sampling occurred during the summer and fall of 2020.

3.1 Remote thermal sensing and relationship to spring discharge

Stationary nadir thermal infrared images were taken (within ~~±~~2 hours of low tide, from an elevation of approximately 60 masl, during clear sunny days) of the springs entering the lagoon throughout July and August 2020. This study used a Matrice 210 RTK v2 aerial drone, equipped with a 13 mm non-radiometric DJI ZENMUSE™ XT2 thermal infrared camera ~~with FLIR technologies~~ (XT2; DJI, 2018). Real-time kinetic processing was used for drone navigation~~, as well as image geotagging, and the position of the images relative to the base station is expected to be highly accurate (<5 cm) even without the use of ground control points~~ (Kalacska et al., 2020). ~~The XT2 has a 45°×37° field of view, 640×512 resolution, 8-bit colour pallet, spectral range between 7.5 and 13.5 µm, sensor sensitive range between -25 and 135°C (*High Gain Mode*), and an absolute thermal accuracy of ±5 to 10°C (DJI, 2018).~~ The ~~a~~exact~~bsolute~~ temperatures of the thermal imagery were not deemed reliable due to internal drift of the sensor, lack of radiometric correction, and disagreement in thermal readings between frames. However, it was assumed that the relative temperature data in each frame were sufficiently precise for the consistent definition of thermal plume geometry, given the reproduceable ability of the XT2 to identify surficial thermal anomalies confirmed with *in-situ* temperature measurements. ~~Rather than developing a per-pixel corrections matrix for the sensor to correct for distortion towards the image periphery, only the central portion of each image was analysed (Kelly et al., 2019a).~~ The image analysis process to identify thermal anomalies and delineate the associated cold-water plumes was based on previous work (e.g., Kelley et al., 2019; Roseen, 2002) and is described in~~the text and figure (S1) at the beginning of~~ the supplementary material (Figs.~~ure~~ S1 and S2).

~~This study applied FLIR Tools®, ImageJ, and MATLAB® to post-process grayscale intensity data from the thermal infrared images using the procedure summarized in Fig. 2. These products enabled the analysis of high-resolution thermal data and polygonal cropping procedures. Grayscale intensity data was extracted from the thermal images of the spring-sourced plumes and graphed with respect to cumulative area to yield a characteristic S-shape type-curve (Fig. S1). Each 'inflection point' of the graph was used to define 'thermal groups' and the sharp transition zones between them (Roseen, 2002).~~ Once the thermal plume areas were delineated, an empirical relationship was developed between discharge measurements for a subset of springs (Sect. 3.2) and their ~~area of spring thermal plumes determined from the graphical analysis~~thermal plume areas (e.g., Danielescu et al., 2009). This plume ~~size~~area-spring discharge relationship was then applied to estimate the *instantaneous* discharge of ungauged springs from their respective thermal plume areas captured by drone thermal imagery. *Continuous* spring discharge to the lagoon was estimated for the focused study period using a hydrologic proxy (e.g., Danielescu et al., 2009). Herein, the water levels in our near-shore piezometer (Fig. 1b and Section 3.2) were used as a proxy for the aquifer-lagoon hydraulic gradient and spring discharge (based on Darcy's Law) via proportionality constants developed from the drone-based instantaneous discharge estimates (i.e., discharge was assumed to vary linearly with piezometer water table). Approximately 20% of the lagoon's north-western shoreline could not be surveyed with the drone based on proximity to the road or power lines (Fig. 1), but the presence of springs along this unsurveyed portion has been confirmed by distant thermal images and *in-situ* measurements. Consequently, the total spring discharge to the lagoon was estimated by extrapolating the average spring discharge per shoreline length obtained from the surveyed segments (80%) to the unsurveyed segment (20%).

3.2 Hydroclimatic, thermal, and radon monitoring

The manufacturer, model, location, and monitoring durations for each logger are listed in Table S1, and locations are shown in Fig. 1. A climate station ~~(Onset Hobo Micro Station Logger)~~ was installed at the study site to measure downwelling shortwave radiation, windspeed, rainfall and air temperature. ~~Also, s~~Subsurface modelling and hydraulic assessments were guided by *in-situ* ~~field measurements of subsurface properties~~groundwater monitoring using a shallow groundwater piezometer (5 masl; Fig. 1b~~). The piezometer~~) that fully penetrated the surficial soils to a depth of 4.5 m. This lowland well was instrumented with a pressure transducer to monitor well recovery during a slug test, as well as to provide a record of ~~water table dynamics~~groundwater elevation, temperature, and electrical conductivity. Water stage was monitored at 15-minute intervals in the four primary streams (S1 to S4; Fig. 1b) over the study period using pressure transducers corrected with air pressure data from the nearest ECCC climate stations (Station IDs 41903 and 7177; ECCC, 2021a, 2021b). Stream discharges were measured ~~via the velocity-area (Dingman, 2002, p. 609) method~~ using an acoustic Doppler velocimeter ~~Sontek~~

~~FlowTraker2® (Xylem Inc, Rye Brook, New York, USA)~~ and were used to generate rating curves for local streams (average n = 6 and $R^2 = 0.94$). Other smaller streams (S5 and S6, Fig. 1b) were gauged intermittently, but their flow rates were < 1% of the combined flow of streams S1 to S4 and are thus hereafter not considered. Considering the limited amount of precipitation (36 mm) over the 35-day focused study period (July 23 to August 26, 2020), streamflows were assumed to be entirely baseflow. This simplification will be ~~assessed~~ discussed later but is not anticipated to introduce significant error because PEI streams have frequently been documented to be 80-100% baseflow during the summer (Benson et al., 2007; Brandon, 1966).

A spring thermal plume area-~~spring~~ discharge relationship (Sect. 3.1 and box 3, Fig. 2) in tidal zones is only valid for a point in time (i.e.~~e.g.~~, for a given tidal stage/current and atmospheric conditions) as the thermal and hydraulic mixing are highly sensitive to environmental conditions (KarisAllen and Kurylyk, 2021). Accordingly, we were only able to manually gauge three springs at approximately the same time as the lagoon-scale thermal mapping~~, was~~ conducted on July 22, 2020.~~ XX.~~ The environmental conditions were ideal for plume mapping and flow gauging on this date given the high (spring) tidal range that fully exposed the intertidal springs and the concurrent heat wave that maximized the thermal offset between the groundwater and lagoon~~ temperatures.~~ ~~To develop relationships between spring discharge and thermal plume area (Sect. 3.1), volumetric~~ Volumetric flow measurements for these three springs (Figs. ~~S2, S4~~S3, S5, yellow rings) were conducted at low tide by constructing custom weirs surrounding their respective outlets. ~~Three springs were chosen to represent the range of anticipated spring discharges to the lagoon. Volumetric measurements of springs were made with an accuracy of ±10 mL, but flows were not entirely captured at the spring outlet due to limitations with the water collection technique and outlet geometry.~~ To remove any tide-circulated saltwater from our spring discharge estimates (LeRoux et al., 2021), the freshwater component discharging from the spring was isolated by estimating saltwater content via a simple two-component electrical conductivity mixing model ~~based on the electrical conductivities of the spring, lagoon, and shallow fresh groundwater~~~~conductivity~~. Importantly~~, as discussed later~~, while we only gauged three springs, the thermal plume areas for these springs span the range of ~~all of~~all the mapped thermal plume areas but one. Thus, discharge rates for ungauged springs are generally interpolated rather than extrapolated from the plume area-discharge relationship.

Additional instruments were installed throughout the lagoon and watershed (Fig. 1~~b~~) in tandem with stream monitoring work to investigate water quality and hydrologic/hydrodynamic processes. Temperature sensors were installed at multiple locations along the lagoon channel at the top (affixed to a buoy) and bottom (affixed to an anchor) of the water column, three springs outlets (i.e., Springs 2, 5, and 21; Figs. ~~S2~~ S3~~to S5~~, blue rings), and the four primary streams (Streams S1-S4) to characterize their thermal regimes. Spring temperatures patterns (i.e., seasonal amplitudes) were compared to the results of the thermal numerical modelling (Sect. 3.3) to estimate the aquifer source depth for a given spring following the effective aquifer depth approach of Kurylyk et al. (2015b) and Briggs et al. (2018). ~~Also, t~~The paired spring flow and temperature data were used to quantify net (sensible) advective heat fluxes to the lagoon over the focused study period (Kurylyk et al., 2016):

$$J_{adv,i} = C_w Q_{input}(T_{input} - T_{lagoon}), \quad (1)$$

where J_{adv} is the net (sensible) advective water energy flux (W), C_w is the volumetric heat capacity of water (J m^{-3} °C^{-1}),

Q_{input} is the input (direct rainfall, spring, or stream) water discharge (m^3 s^{-1}), T is the water temperature (°C), T_{input} and T_{lagoon} are the water temperatures for the hydrologic input (rainfall, spring, or stream) and lagoon, respectively. Precipitation temperature was assumed to be the same as the average air temperature from the climate station over the short, focused study period.

Advective heat fluxes for the springs and streams were considered ~~to integrate the hydrology and thermal investigations in this study and~~ to investigate the springs' thermal function ~~in the lagoon~~at the scale of the lagoon. A complete lagoon energy balance cannot be completed due to a lack of complete surface energy flux data and data for the hydraulic and thermal exchange with the ocean. However, as a first-order estimate of the relative thermal effects of the freshwater inflows at the lagoon scale, the advective fluxes obtained via Eq. (1) were compared to the downwelling shortwave radiation ~~-~~(W m^{-2}) measured at the study site climate station (Fig. 1) and multiplied across the lagoon surface area.

~~An electrical conductivity logger was installed in the largest stream (S1).~~ Conductivity-temperature-depth loggers ~~(Solinst Levelogger® 5 LTC)~~ were installed within the lagoon and in two intertidal springs (summer 2020 only). Discrete water temperature and electrical conductivity measurements of the lagoon, springs, streams, and piezometer were also taken during field investigations using handheld devices (Apera EC400S Portable ~~Conductivity/TDS/Salinity/Resistivity~~ Meter and a YSI ProDSS ~~Multiparameter Digital Water Quality Meter~~) ~~and a Solinst LTC logger~~ to parameterize the two-component salinity mixing model used to correct the estimations of freshwater discharge from gauged springs.

Dissolved radon (^{222}Rn; $t_{1/2}$ = 3.83 d) is naturally enriched in groundwater and is an inert noble gas, making it an effective tracer for groundwater discharge to coastal systems (Swarzenski, 2007). Four groundwater springs were sampled for ^{222}Rn in August and November 2020 (Fig. 1b) coincident with continuous paired electrical conductivity, water depth, and temperature monitoring as previously described. Glass bottles (250 mL) were submerged directly at the spring outlet and allowed to overflow, collected bubble-free without headspace, and analysed via RAD-H2O (Durridge Co.). Stream surface waters and shallow lagoon pore waters were additionally analysed in November (Fig. 1b). Near the inlet of Basin Head lagoon, surface water was continuously drawn into a gas exchange chamber (RAD-AQUA), and ^{222}Rn was monitored using a commercial radon-in-air monitor (RAD7, Durridge Co.) over 24 hours in August (Fig. 1b, southernmost blue ring)**.** Dissolved ^{222}Rn activities were determined using the solubility constants from Schubert et al. (2012) for temperature and salinity and corrected for instrument response delay.

A mass balance model was developed for ^{222}Rn (Burnett & Dulaiova, 2003; Rodellas et al., 2021; Sadat-Noori et al., 2015):

$$J_{mix} + J_{decay} + J_{atm} = J_{spring} + J_{stream} + J_{diff} + J_{Ra-226}, \quad (2)$$

where J represents the flux of ^{222}Rn (Bq d^{-1}) for all known sources (baseflow-fed streams J_{spring}; molecular diffusion J_{diff}; ^{226}Ra production J_{Ra-226}) and sinks (mixing J_{mix}; radioactive decay J_{decay}; atmospheric evasion J_{atm}) of ^{222}Rn within the Basin Head lagoon. With the time-series monitoring station near the inlet of the lagoon, we assume that this point-in-space is representative of all ^{222}Rn inputs and outputs through the tidal inlet and thus any imbalance between known sources and sinks is attributed to unknown groundwater inputs (J_{spring}). This estimate provides a maximum range of groundwater inputs (Peterson et al., 2010), and includes both focused (spring) and diffuse groundwater discharge~~/circulation~~, in contrast with the thermal plume method (springs only).~~.~~

3.3 Groundwater and thermal numerical modelling

Ground temperature modeling for present and future conditions was used to interpret ~~the~~ field data and to project future groundwater warming~~ scenarios~~ (box 6, Figure 2). A 1-D subsurface heat and water transport model was developed and manually calibrated to local groundwater temperature observations, with hydrologic parameterization informed by local data (e.g., weather data, piezometer slug test) and literature values, and calibrated using measured groundwater temperature data from the piezometer (Figure 1) and an upland well~~, as described later (Section #)~~ (see Section 4.3.1). Downscaled future climate projections were then applied as upper boundary conditions to drive simulations of plausible future subsurface temperatures, with the goal of assessing the potential sensitivity of springs to projected multidecadal warming trends (Fig. 3a). The conceptual complexity of the numerical model was limited both to facilitate model parameterization as well as interpretation; nevertheless, this approach preserved key heat transport processes. Multi-dimensional systems such as the fractured sandstone/mudstone aquifers feeding the intertidal springs in the Basin Head lagoon may be simplified into a one-dimensional system operating on the concept of an 'effective aquifer depth', which lumps together multi-dimensional processes and can be derived by relating the amplitude decay or phase shift of the seasonal groundwater temperature sinusoid relative to the air temperature signal (Kurylyk et al., 2015b). One-dimensional heat transfer modeling approaches have been used in previous studies considering groundwater thermal impacts on rivers (e.g., Briggs et al., 2018a, b) and in analytical solution studies of past or future groundwater warming (e.g., Gunawardhana et al., 2011; Irvine et al., 2017). The thermal regimes of shallow aquifers exhibit a depth-dependent response to seasonal surface temperature signals~~ and climate change~~, and thus the measured seasonal amplitude of groundwater discharge temperature yields an approximate average groundwater depth (Kurylyk et al., 2015b) that can be used to estimate the thermal response of that spring to multi-decadal warming.

The selected ~~numerical~~ model, Simultaneous Heat and Water model (SHAW; Flerchinger & Saxton, 1989), simulates transient vertical energy and water transport through a canopy, snow layer, plant residue, and soil layers (Flerchinger, 2017). The robust physical basis and ability of SHAW to simulate the surface energy balance, snowpack, vegetation, and seasonally frozen soil processes (e.g., Mohammed et al., 2017) made it an appealing choice for this long-term thermal study, as these processes affect subsurface thermal trends at the latitude of the study site. A description of model processes and equations, as well as the boundary condition options, are detailed in Flerchinger (2017)~~,~~ and summarized here. The surface temperature (land, vegetation, or snow) is obtained by balancing the surface heat fluxes (net all-wave radiation, turbulent fluxes of sensible and latent heat, ground heat flux). Vertical heat transfer through the snowpack, vegetation, organic material, soil, and deeper subsurface layers is simulated with partial differential equations for energy transport. For the soil (ground) layers, the one-dimensional, transient conduction-advection equation in SHAW is:

$$C_a \frac{\partial T}{\partial t} - L_i \rho_i \frac{\partial \theta_i}{\partial t} = \frac{\partial}{\partial z}\left[\lambda_e \frac{\partial T}{\partial z}\right] - \rho_w c_w \frac{\partial q_w}{\partial z} - L_v \left(\frac{\partial q_v}{\partial z} + \frac{\partial \rho_v}{\partial t}\right) \qquad (3)$$

where C_a is the bulk volumetric heat capacity of the soil (J m^{-3} C^{-1}), T is soil temperature (°C), L_i is the latent heat of fusion (J kg^{-1}), ρ_i is the ice density (kg m^{-3}), θ_i is the soil ice content (m^3 m^{-3}), λ_e is the bulk soil thermal conductivity (W m^{-1} C^{-1}), ρ_w is the water density (kg m^{-3}), c_w is the water specific heat capacity (J kg^{-1} C^{-1}), L_v is the latent heat of vaporization (J kg^{-1}), q_w is the soil water flux (m s^{-1}), ρ_v is the vapor density in the soil (kg m^{-3}), and q_v (kg m^{-2} s^{-1}) is the soil vapor flux. Water balance and vertical fluxes are computed in a similar manner using a partial differential equation based on mass balance rather than energy balance (Flerchinger, 2017). SHAW has been successfully and widely applied in a range of environmental conditions to simulate subsurface temperatures.

~~Standard values were employed for the thermodynamic properties of water (Flerchinger and Saxton, 1989).~~ Bulk thermal properties of the subsurface in SHAW are estimated based on the approach of DeVries (1963) by using user-input soil compositions and model-computed water content; soil compositions were herein based on local soil surveys and historical studies of PEI soils (e.g., Crowl, 1969a). This study separated the model domain into an unsaturated upper region (0 to 3 m depth) that computed the upper boundary condition and forcing to the lower, saturated region model (3 to 93 m depth; Fig. 3b). The bottom boundary position was selected (after various iterations) to ensure that the lower boundary did not influence the thermal sensitivity of the shallow groundwater temperatures, which were the focus of the present study. SHAW version 3.0.3 was used for the upper domain to calculate surface and vadose zone ~~processes~~fluxes, whereas a modified version of SHAW 2.4 was used for the lower region to exclusively consider subsurface thermal transport below the water table without solving the surface energy balance (Mohammed et al., 2017).

Climate inputs required by SHAW to solve the surface energy balance for the upper region model include maximum and minimum daily air temperature, dew point temperature, wind speed, total precipitation, and all-sky radiation. The timestep, input data, and output of the simulations had a daily resolution as in other groundwater temperature studies using SHAW (e.g, Langford et al., 2020). Ground(water) temperatures in saturated conditions are relatively easy~~relatively easier~~ to simulate compared to soil moisture, which enables the coarser timestep compared to models focusing on reproducing soil moisture variations. Based on the period of this study and the availability of historic data and climate projections, historical simulations were conducted over 37 years (1984-2020), and future simulations were run over 81 years (2020-2100). The minimum and maximum air temperatures, as well as total precipitation for the historical simulations, were sourced from the CNRM-CM5, RCP4.5 hindcast model (Voldoire et al., 2013), which more accurately reproduced historical conditions for PEI~~ locations~~ relative to other climate simulations (Warner, 2016). There is no direct long-term climate record for the study site (Basin Head), and, given our focus on multi-year averages in groundwater temperature, we are not concerned with high-frequency differences between hindcast data and actual environmental conditions. Thus, we used the hindcast data for our historical period (1984-2000). Data for the hindcast and projections were statistically downscaled to a ~ 10km grid size (ECCC et al., 2021). Local dew point temperature, wind speed at 2 m above ground level, and all-sky solar radiation data were sourced from the NASA POWER reanalysis database (Sparks, 2018). As there were no readily accessible future projections for dew point temperature, wind speed, and all-sky solar radiation, these were estimated by repeating data from a portion of the historical period (i.e., 1985-2020; Sparks, 2018). The repeating of these data is not expected to produce significant errors given the relative hydraulic and thermal inertia of groundwater systems and because groundwater temperature changes are later interpreted herein using 5-year averages to smooth out any short-term effects. Future daily maximum air temperature, minimum air temperature, and total precipitation to drive future model projections were sourced from four climate simulations based on work by Warner (2016): (1) CNRM-CM5, RCP4.5; (2) CNRM-CM5, RCP8.5; (3) MRI-CGCM3, RCP4.5; and (4) MRI-CGCM3, RCP8.5 (ECCC et al., 2021). ~~Simulated temperature at 3 m in the upper region model was then used as the upper boundary condition for the lower saturated model (Fig. 3b).~~

4 Results

4.1 Remote thermal sensing and spring discharge analysis

Based on cold-water plumes visible in the drone-based aerial thermal imagery (e.g.,~~see~~ Fig. 4~~ for examples~~), 40 springs were located on the north and west shores of the lagoon (mapped in Fig. 1b and Figs. S2-S6 of supplement). ~~These are mapped in Fig. 1b, with enhanced zoom and labels in Figs. S2~~S3~~-S5~~S6~~. Selected springs identified from the thermal imagery were gauged (Table S2) to develop a plume size-discharge relationship (Fig. 5d and Sect. 3.1-3.2). Electrical conductivity values for the low-low tide discharge measurements of the three gauged springs~~ (Sect. 3.1, 3.2) ~~and the associated end-member analysis revealed that s~~Spring discharges ~~at the times of measurement ~~were <2% saltwater, determined from electrical conductivity, so the resultant freshwater correction had a minimal effect on discharge estimates (Sect. 3.1, 3.2). The paired discharge values and thermal plume areas for these three gauged springs yielded a power function thermal plume area-discharge relationship for the lagoon at this point in time (R^2=0.99; Fig. 5d).

The areas of only 34 springs were graphically assessed using ~~low-~~low-tide thermal image pixel data (Table S2) because the remaining identified springs were either too small or inaccessible for close imaging via the drone. The results and workflow ~~and resulting~~for the plume area associated with Spring 8 is shown as an illustrative example in Fig. 5. Instantaneous spring discharges for ungauged springs (Springs 1-31; Table S2) were computed as a function of plume area using the lagoon power function (Fig. 5d). ~~Only Spring 1 had a larger plume size than the largest gauged spring (Table S2), indicating that the discharge values for the springs were generally constrained by the area range in our empirical plume area-discharge relationship.~~ The estimation of continuous spring discharge over the focused study period from the instantaneous spring discharges via the proxy data (i.e., piezometer water level, Sect. 3.2) yielded a total spring discharge volume estimate for this 35-day period of 113,000 m^3 (0.037 $m^3 s^{-1}$). Springs were found at a density of approximately six springs per kilometre along the surveyed section, which yielded ~~an estimate of~~ approximately 580 m^3/km/day (0.0067 m^3/s/km) for the discharge rate per shoreline length. Assuming a ~~constant~~ similar spring flow ~~and density~~per length for the 20% unsurveyed shoreline resulted in a cumulative ~~estimated~~ 35-day total spring discharge of 142,000 m^3 (0.047 $m^3 s^{-1}$).

4.2 Hydroclimatic monitoring data and analyses

4.2.1 Stream discharge monitoring results

Stream monitoring data (Fig. ~~S7~~S8) were analysed to estimate the total indirect groundwater flow (baseflow) to the lagoon during the focused study period, which yielded the following inflow volumes (flows): S1 = 90,000 m^3 (0.030 $m^3 s^{-1}$); S2 = 22,000 (0.0073); S3 = 33,000 (0.011); and S4 = 7,700 (0.0025). Based on the assumption that all streamflow is baseflow during the summer months as supported by the lack of flow 'spikes' (Fig. ~~S7~~S8) and typical summer conditions in PEI, streams contributed approximately 153,000 m^3 (0.050 $m^3 s^{-1}$) of indirect groundwater to the lagoon over the focused study period. This total streamflow is within 6% of the total spring inflow estimated from the thermal analysis, suggesting the two hydrologic pathways for groundwater delivery (baseflow and spring discharge) are comparable at this site in the summer.

4.2.2 *In situ* temperature data

Water temperatures in the lagoon were relatively high during the focused study period (maximum 15-minute temperature of 33°C), with mean daily water temperatures often greater than the mean daily air temperatures and occasionally exceeding 25°C in the northeast arm of the lagoon (Fig. 6). In contrast, the groundwater-dominated streams had mean daily water temperatures between 10°C and 14°C during this period, and groundwater discharge temperatures remained between 7 and 10°C for all continuously monitored springs (Figs. 6, 7). Seasonal lagoon water temperatures peaked in late July to early August. Lagoon and stream temperatures exhibited at least limited diel variability (hourly data, Fig. ~~S8~~S9), whereas none of the monitored springs displayed diel temperature trends once tidal effects were removed. Over the focused period, the median 15-minute water temperatures and interquartile ranges (IQR) of Stream S1, S2, S3 and S4 were 8.7°C (IQR = 0.6°C), 10.8°C (IQR = 1.2°C), 10.5°C (IQR = 1.3°C), and 10.4°C (IQR = 1.0°C), respectively. Stream temperature measurements were taken near the stream mouths (above normal head of tide, Fig. 1) and represent the outcome of the cumulative upstream heat exchange, including the surface heat fluxes absorbed along the channel. T~~; t~~his caused~~ that contributed to the~~ stream temperatures ~~exceeding the~~ to exceed spring temperatures in the summer months (Figs. 6 and ~~S8~~S9). Five temperature sensors distributed throughout the lagoon (Fig. 1b) over the focused period yielded a higher temperature median (~22°C) and variability (IQR = 4°C). Temperatures were typically greatest in the shallower, more poorly flushed upper reaches of the northeast arm of the lagoon and lowest in the deeper main basin (Figs. 1b, 6).

Summertime lagoon water temperatures over the study period were consistently lowered surrounding spring outlets~~, enabling the drone-based analysis in this study~~; however, the extent of these thermal anomalies varied substantially with tidal stage and channel geometry (KarisAllen & Kurylyk, 2021). The difference between coincident spring and lagoon temperatures was up to 23°C (Fig~~ure~~. ~~S8b~~S9b). The thermal patterns of three springs (Fig. 7) were analysed to estimate their seasonal signal properties (especially amplitude) and by extension their relative depth and vulnerability to climate warming by comparison to the modeled results. Temperatures at each of the spring outlets (Fig. 7) exhibited pronounced semi-diurnal oscillations (i.e., 12.42 hr periods) due to the altered aquifer-lagoon hydraulic gradients and enhanced lagoon mixing at higher tide. ~~The stability of the actual groundwater discharge temperature over tidal periods was confirmed by one sensor buried slightly deeper (5-10 cm) in Spring 3 that only exhibited seasonal variation (not shown).~~ To isolate the groundwater temperature from the time series at the spring outlets, the temperatures at low tide over several months of tidal cycles were fitted with an annual (period = 1 year) thermal sinusoid (red dashed lines, Fig. 7). The average temperature of Spring 5 was 7.65°C (Fig. 7a). The lack of thermal periodicity in this spring suggests that its source depth is below the extinction depth of annual air temperature patterns (normally 10-20 m in this region, e.g., Kurylyk et al., 2015b). In contrast, Spring 21 (Fig. 7b) displayed an annual signal with a mean of 7.75°C and an amplitude (half the range) of 1.6°C. Spring 2 also displayed a seasonal signal (Fig. 7c) with the lowest mean temperature (7.05°C) and ~~the~~ highest amplitude (2.0°C). This amplitude suggests that Spring 2 has the ~~shallowest~~ lowest source depth and is the most vulnerable to multidecadal warming of the three springs investigated, as discussed later~~ (Section .##).~~ The fitted spring annual temperature amplitudes were ~~later~~ compared to depth-variable seasonal results from numerical modelling to infer approximate average depths of the groundwater delivered to the springs (Sect. 4.3.2).

4.2.3 Lagoon heat fluxes

Selected advective components of the Basin Head lagoon heat budget associated with freshwater inflows were estimated for the 35-day focused study period (Table 1). Continuous spring discharge for the net advection calculation was estimated from the water table proxy approach (Sect. 3.2). The freshwater inflows from the precipitation, streams, and springs cooled the lagoon water temperature over the summer, as indicated by their negative net thermal advection values (Eq. 1) in Table 1. The estimated total net advective heat flows for the streams and springs were almost identical and over an order of magnitude higher than the advection from direct precipitation. Any unquantified diffuse groundwater input (upwelling to lagoon) would further increase the relative contribution of direct groundwater on the lagoon heat budget. As expected, heat flow from downwelling solar radiation was substantially larger than advective heat components to the lagoon (Table 1), suggesting that the springs and streams likely exert minor influence on the average water temperatures throughout the lagoon, despite their evident thermal impact at a localised scale along the shoreline (Figs. 4 and S8). A heat budget, including advective exchanges with the ocean and a complete surface energy balance, is required to gain a full understanding of the relative thermal effects of these freshwater inflows at the scale of the full lagoon, but data are not available for many heat flux components.

4.2.4 Radon results

Near the lagoon inlet, surface water ^{222}Rn activity varied from 10 to 97 Bq m^{-3}, with maximum activities occurring near low tide when salinities were lowest, and following classic hysteresis loops (Figs. 8a, b). The ^{222}Rn activities~~y~~ of the fractured sandstone springs (10,400 ± 3,700 Bq m^{-3}; n=4) were an order of magnitude higher than for the shallow, brackish porewaters (630 ± 250 Bq m^{-3}; n=4) and baseflow-fed streams (1,100 ± 1,200 Bq m^{-3}; n=4) as shown in Fig. 8a and Table S3. Stream discharge during the surveyed period, 0.05 m^{3} s^{-1}, results in a stream-derived radon flux of (4.7 ± 5.6) × 10^{6} Bq d^{-1}. This flux represents a theoretical maximum, as there will be appreciable ^{222}Rn degassing and decay within the stream prior to entering the lagoon. Based on the minimum observed ^{222}Rn concentration (Gilfedder et al., 2015), the diffusive flux of ^{222}Rn may be approximated as 11 ± 6 Bq m^{-2} d^{-1}; or (6.4 ± 3.2) × 10^{6} Bq d^{-1}, over the total lagoon area. Losses of ^{222}Rn due to tidal mixing (Burnett & Dulaiova, 2003) and atmospheric evasion (MacIntyre et al., 1995) are taken as the mean (± standard deviation) losses estimated over the 24-hour tidal cycle, upscaled to the lagoon surface area (Table S4). Similarly, radioactive decay is estimated considering the mean excess ^{222}Rn inventory, for a net loss of (1.9 ± 1.6) × 10^{6} Bq d^{-1}. Considering known sources and sinks, there is an excess of ^{222}Rn (8.0 ± 6.0 × 10^{7} Bq d^{-1}) attributable to groundwater. Using a ^{222}Rn endmember from the fractured-sandstone springs (10,400 ± 3,700 Bq m^{-3}), we estimate maximum groundwater inputs of 0.09 ± 0.07 m^{3} s^{-1}. Given our uncertainties, the absolute value of this flux should be interpreted with caution, but it is useful for placing results from other methods into a broader context.

4.3 Groundwater and thermal numerical modelling results

4.3.1 Model calibration and sensitivity

Model ~~parameters~~ elements (e.g., residue layer, organic content, water table depth, and snow/rain threshold) were manually calibrated within appropriate ranges to improve agreement of the historical simulation with the approximate calibration targets ~~(e.g., residue layer, organic content, water table depth, and snow/rain threshold)~~. ~~A fixed water table depth of 3 m relative to ground surface was assumed based on this the piezometer's monitoring data over the study period (June 2019 to November 2020).~~ The SHAW model was manually calibrated to the mean, amplitude, and lag ~~subsurface temperatures measured in this piezometer, as well as the amplitude attenuation and lag~~ of the ~~annual~~ seasonal groundwater temperature signal ~~relative to the air temperature signal.~~recorded in the transducer in the coastal piezometer (4.24 m below surface), and modeled and measured results were in agreement post calibration (Table S5). ~~The relative sensitivity of modelled subsurface temperatures to the tested~~

~~calibration elements were documented (REF). The piezometer sensor was at a depth of 4.24 m below surface and recorded groundwater temperatures between 5.10 and 9.50°C, annual amplitudes between 1.80 and 2.20°C, and a lag of 70 to 100 days relative to the annual air temperature signal based on 2019 and 2020 data. The outputs of the calibrated historical simulation were in reasonable agreement with the piezometer data. The range of mean annual temperatures, as well as the amplitude and lag of the thermal signal at each depth were calculated using the final 5 years of the historical simulation (i.e., 2016-2020). At 4.2 m depth, the modelled 2016-2020 mean annual groundwater temperature was between 7.45 and 7.8°C, the amplitude was 2.1 to 2.2°C, and the lag was 92-105 days.~~ Furthermore, after accounting for the difference in water table depth, ~~modelled~~ outputs from the calibrated model at 13.9 meters depth were in agreement with temperature measurements at the same depth in a nearby upland provincial observation well (~~(~~Souris Line Road observation well at 55 masl; Government of PEI, 2021 and Table S1 footnote). Relative model uncertainty results are presented in Table S6.

4.3.2 Historic and future simulation results

The atmospheric forcing (Fig. ~~10~~9a) and the SHAW-modelled subsurface temperature response (Fig. ~~10~~9b) over the last five years (2016-2020) of the historical simulation are presented for different depths to illustrate the intra-annual variability of temperature and the attenuation and lagging of the surface temperature signal with depth. The modeled amplitudes of the annual temperature signals (Fig. ~~10~~9) may be compared to the measured spring outlet thermal patterns (red lines, Fig. 7) to estimate the springs' effective source depths (Kurylyk et al. 2015b). Based on their annual amplitudes, Springs 2 and 21 are likely predominantly sourced from effective depths between 3 and 7 m. ~~, whereas~~ Spring 5 is interpreted to be ~~predominantly~~ fed from depths below 12 m, although we recognize that springs are sourced the convolution of flows from different depths.~~,~~

The final 5 years of the future simulations (2096-2100) were compiled and compared to the final 5 years of the historical simulation (2016-2020, Table 2) to assess future groundwater warming. The subsurface temperatures at 4.2 and 13.9 m (~~piezometer and government well~~ sensor depths in piezometer and government well) increased with increasing atmospheric and surface temperatures in all simulations (Fig. 9). ~~Modelled~~ For example, focusing on the model calibration/assessment depths for the piezometer and monitoring well reveals that modelled groundwater temperature is projected to increase by 0.08 to 2.23°C at 4.2 m depth and by 0.~~32 to 1.42~~45 to 1.62°C at 13.9 m (Table 2), indicating the depth-dependency of warming for a given timeframe and the influence of a given climate scenario. The MRI-CGCM3, RCP 8.5 simulation had the greatest temperature increase, ~~and~~ whereas the MRI-CGCM3, RCP 4.5 simulation had the lowest (Table 2).

~~The atmospheric forcing (Fig. 10a) and subsurface temperature response (Fig. 10b) over the last five years (2016-2020) of the historical simulation are presented for different depths to illustrate the intra-annual variability of temperature and the attenuation and lagging of the surface temperature signal with depth. The modeled amplitudes of the annual temperature signals (Fig. 10) may be compared to the measured spring outlet thermal patterns (red lines, Fig. 7) to estimate the springs' effective~~

~~source depths (Kurylyk et al. 2015b). Based on their annual amplitudes, Springs 2 and 21 are likely sourced from depths between 3 and 7 m, whereas Spring 5 is interpreted to be predominantly fed from depths below 12 m.~~

The SHAW modeling indicates that the springs with more seasonally stable temperatures are sourced from greater depths (Fig. 9b) and will thus experience delayed warming due to climate change (e.g., Fig. 10a vs. 10b). ~~The notion of diverse (i.e., depth-dependent) spring thermal sensitivities is further supported by comparing the warming rates at different depths within the soil column.~~ For example, 5-year averaged air temperature is simulated to increase by approximately 4.32°C over the course of the warmest future simulation (i.e., MRI-CGCM3, RCP8.5). ~~This~~ This ~~air temperature signal~~atmospheric warming increased the 5-year averaged groundwater temperature by approximately 1.78°C at 4.2 m depth and 1.57°C at 13.9 m depth. For relative comparison, this suggests a relative (to air) groundwater warming rate (or 'thermal sensitivity') of 0.41°C/°C at 4.2 m depth and 0.36°C/°C at 13.9 m depth ~~per 1°C of air temperature rise~~ by the year 2100, although the differences can be higher between these locations for a given year (see range in Table 2).~~.~~ The model results also illustrate that shallower aquifer zones are more vulnerable to short-term (seasonal and inter-annual) variations in temperature given how the seasonal amplitude and year-to-year variation are reduced with depth ~~(see Fig. 9a,b and 10b)~~ (Figure 9b). Thus, short-term and long-term dynamics are more pronounced in the shallower springs, causing them to reach higher peak temperatures in a given year.

5 Discussion

5.1 Thermal plume analysis and continuous discharge estimation

This study applied a power curve regression to the collected spring discharge and area data, which varies from previous studies that have applied linear (e.g., Bejannin et al., 2017; Lee et al., 2016b; Tamborski et al., 2015) or logarithmic relationships (Danielescu et al., 2009). Our high coefficient of determination ($R^2 = 0.99$, Fig. 5d) suggest a strong relationship between plume size and discharge, although we concede this is based on a limited number of points for reasons ~~already~~ discussed ~~on limited points~~. ~~Also, p~~Previous studies have converted instantaneous discharge measurements based on thermal plume analysis to continuous discharge estimates by using baseflow as a proxy for spring discharge (Bartlett, 2011; Danielescu et al., 2009). Rather than baseflow, we used groundwater levels measured in a piezometer ~~relatively~~ close to the lagoon as this was thought to be a better proxy for the local hydraulic gradient (and thus spring flow) than baseflow which integrates processes further up-catchment.

To overcome limitations with the limited number of points informing the thermal plume area-discharge relationship and the associated total spring discharge estimate of 0.047 $m^3 s^{-1}$, we independently assessed total groundwater inputs using a ^{222}Rn mass balance. Assuming that groundwater discharge to the lagoon accounted for the differences between known ^{222}Rn sources and sinks, maximum input of groundwater was estimated as 0.09 ± 0.07 $m^3 s^{-1}$ (Table S4). Given the uncertainty of both approaches, these independent assessments are quite comparable. Also, the ^{222}Rn approach may capture additional diffuse groundwater inflows not captured by the drone survey, and thus it is expected the discharge from the radon approach would be higher. For example, Danielescu et al. (2009) found that approximately 25% of groundwater inflow to two PEI coastal systems was diffusive, and such inflows were not accounted for in the drone thermal imagery analysis in this study. The results reveal the value in using complementary but independent estimates of groundwater inflows from different types of tracers (~~herein~~ heat and radon), particularly if both estimates are highly uncertain.

The comparison of estimated streams and spring flows from this study reveal that the magnitude of direct groundwater inputs to PEI coastal systems is likely significant relative to stream inputs in the summer. As in other studies (Danielescu et al., 2009), we assumed that intertidal spring discharge measurements taken at low tide were representative of the discharge over the tidal cycle. However, discharge would theoretically decrease at higher stage due to the reduced aquifer-lagoon hydraulic gradient (Lee et al., 2016b; LeRoux et al., 2021), and spring-sourced thermal plumes at this site can be obscured at high tide (KarisAllen & Kurylyk, 2021). This is supported by time-series observations of ^{222}Rn, where maximum activities are observed during ebb and low tides (Fig. 8c). However, relatively low electrical conductivity and temperature around certain springs during high tides suggests that at least some springs discharge continuously.

5.2 Water temperature and heat transfer

The thermal imagery and ~~the~~ *in-situ* temperature time series reveal the contrast between summer 2020 lagoon temperatures (mean ~ 22°C, maximum 33°C) and the stream (8-13°C) and spring temperatures (7-10°C). The relative hydrologic and thermal stability of the streams attest to their groundwater dominance (Kelleher et al., 2012; Mayer, 2021; Johnson et al., 2021). The *in-situ* data and thermal imagery also collectively illustrate that thermally stable groundwater inflows can reduce the *temporal* variability in surface water temperature (streams vs. lagoon temperatures, Fig. 6) and yet simultaneously enhance the *spatial* variability of temperature (lagoon cold-water patches). The influence of groundwater on the lagoon temperature~~,~~ relative to other thermal controls (e.g., tidal exchange, solar radiation)~~,~~ is ~~likely~~ dynamic in space and time. Groundwater inputs may be most significant as a thermal buffer throughout the hottest periods of the summer months when rainfall is scarce and lagoon temperatures and stream baseflow indices peak. ~~It is expected that groundwater influence is more impactful overnight, in the absence of solar radiation, and during low tides when spring discharge is potentially at its greatest and the total volume within the lagoon is reduced.~~ A full lagoon energy budget (e.g., Rodríguez-Rodríguez & Moreno-Ostos, 2006) would improve our understanding of lagoon-scale thermal dynamics and thus the ~~larger-scale~~ significance of groundwater and its sensitivity to climate warming. However, at a local scale, cold-water plumes created by inter-tidal springs can create distinct thermal zonation (e.g., Figs. 4, S8) that ~~could~~ potentially provide thermal relief to aquatic organisms capable of behavioural thermoregulation or to static organisms collocated with the discharge point. While such groundwater-sourced, thermally habitable niches have received considerable attention in freshwater environments (e.g., Torgersen et al., 2012; Sullivan et al., 2021), they are less studied in transitional, coastal waters (Grzelak et al., 2018; Lecher and Mackey, 2018). The identified cold-water plumes are concentrated along the shoreline (Fig. 1, grey circles), indicating that the nearshore zone and associated microecosystems may be more strongly influenced by focused groundwater inflows than the mid-lagoon ~~surface~~ waters.

5.~~2~~3 Modelling implications

Intertidal springs in the lagoon are sourced from different effective depths in the groundwater system(s). Individual springs experience varied thermal forcing based on their associated soil layers, land-use, land cover, and travel paths that dictate their thermal signature and sensitivity to surface temperatures. In this study, a one-dimensional subsurface model was used to demonstrate that springs within the lagoon are expected to warm in response to future atmospheric warming within decades. The reduced groundwater warming compared to atmospheric warming (Sect. 4.3.2 and Fig. 10~~9~~) does not imply that aquifers ultimately attenuate multi-decadal surface warming signals, but rather that there is a lag between a surface warming signal and its subsurface manifestation (Menberg et al., 2014; Bense and Kurylyk, 2017). For example, if the climate warmed to 2100 and then stabilized, the shallow aquifers over a range of depths would eventually be in equilibrium with the new thermal conditions and the associated damping of groundwater warming relative to atmospheric warming would become progressively less apparent. It is also important to note that the lag in groundwater warming in response to climate change is not the same as the lag in response to seasonal forcing (Section 4.3.1), because the lag depends on the period of the forcing signal (e.g., Stallman, 1965). Modelling results suggest that the mean annual temperature of shallower groundwater supplying some springs may warm more than 2°C before the year 2100 (Table 2). The overall distribution of spring source depths would need to be further explored ~~(e.g., with tracers to estimate groundwater residence time)~~ to assess how sensitive groundwater inputs to Basin Head lagoon may be at the lagoon scale, but these modeling results are valuable to understand the present/future system and to inform future research and management initiatives in this Marine Protected Area (~~see~~ Joseph et al., 2021).

~~Our modeling had~~Our modeling had several limitations. For example, we represented multi-dimensional processes in a one-dimensional system (Figure 3) and did not have multi-depth groundwater data available at a single well for model assessment. Model uncertainty arose from uncertainty associated with the conceptual model, the thermal and hydraulic parameters, and the forcing data; however, ground temperature modeling is far more robust than soil moisture or groundwater hydraulics modeling because thermal signals are modulated with depth, and thermal properties are well constrained in comparison to hydraulic ones (Anderson, 2005). In general, c~~C~~onsidering the data availability and modelling objectives, the resulting calibration and model application were considered satisfactory for the investigations described above. However, future work could consider warming in a multi-dimensional aquifer system with responsive water table dynamics or more fully integrate the lagoon within the model domain in a coupled groundwater-surface water thermal modeling framework (e.g., Brookfield et al., 2009). Numerical groundwater models that account for secondary porosity could be used to consider heat transfer within the fracture network and the porous sandstone matrix (Graf & Therrien, 2007).

5.4 Ecological implications of spring warming

Springs are known to support critical groundwater-dependent ecosystems (Cantonati et al., 2020) due to the distinctive conditions (e.g., nutrient levels, dissolved oxygen, salinity, and temperature) at their outlets;~~, and~~ this study focused on their thermal function. The significance of ambient or local lagoon temperature changes may be contextualized by species-specific temperature thresholds related to metabolic activity and survival. Optimal temperature for giant Irish moss is likely between 8 to 20°C (Bird et al., 1979; Mathieson & Burns, 1971; Tasende & Fraga, 1992), and temperatures above 30°C are highly detrimental (Kübler & Davison, 1993; Lüning et al., 1986). Furthermore, blue mussels (*Mytilus edulis*) provide essential anchorage to giant Irish moss (DFO, 2009; Joseph et al., 2021), and water temperatures ~~between~~ above 25~~-33~~°C may encumber their growth and resilience to predation (Dowd & Somero, 2013). Increasing lagoon temperatures may also be anticipated to alter primary production and macroalgae bloom dynamics (Wells et al., 2020), as well as species distributions and interactions (Anderson, 2013). Consequently, warming of aquifers, and thus springs and groundwater-dependent streams, could negatively impact thermally vulnerable species, as mixing of groundwater into the lagoon results in lower summertime water temperatures at least locally and at low tide (Figs. 4 and ~~S8~~S9). Also, fish have been observed aggregating in these cold-water plumes during warm days, perhaps suggesting that they are being used as refuges by ~~for by~~ thermally stressed aquatic species. Even with the groundwater warming presented in Table 2 and Fig. ~~9~~10, discrete cold-water plumes will still be evident at the mouths of these springs in a warmer climate. However, in general, for a given spring and point in time, the plume volume under key temperature thresholds will be reduced by the multi-decadal warming in the aquifer and, presumably, the lagoon. In summary, ~~as~~because the ~~thermal plumes in the~~ drone imagery indicates that the thermal influence of certain springs and streamss extends ~~extends~~ well beyond their outlets, spring warming and resultant plume warming could influence ecosystem complexity and dynamics within the broader lagoon in the coming decades.

6 Summary and conclusions

Groundwater-dependent coastal ecosystems are largely unexplored in the literature. This study used hydrologic and thermal monitoring, groundwater tracers (temperature and radon), and numerical modelling to explore groundwater discharge and its present and future roles in maintaining survivable temperatures for the threatened ecosystem in the Basin Head Marine Protected Area in southeastern Canada. The cold-water plume areas as revealed in drone-based thermal imagery were used to extrapolate the flow from three gauged springs to 31 ungauged springs. The~~, and the~~ cumulative spring inflow (0.047 m^3 s^{-1}) estimated from this empirical approach was comparable to the total groundwater inflow (focused and diffuse, 0.09 m^3 s^{-1}) yielded from a ^{222}Rn mass balance. The results also revealed that the total spring flow was comparable to the total streamflow (0.050 m^3 s^{-1}), suggesting that, at least at a local level, springs can provide an important pathway for delivering freshwater and energy to coastal zones. Based on a comparison to downwelling solar radiation, advection due to spring discharge exerted little influence on the lagoon-scale heat budget; however, thermal imagery indicates that the shoreline thermal regime is strongly influenced by groundwater discharge. The resultant thermal heterogeneity can provide thermal refuges to support a range of temperature tolerances in a complex ecosystem.

A subsurface heat transfer model parameterized and calibrated with field data was employed to investigate ~~the~~ groundwater thermal sensitivity to seasonal cycles and multi-decadal climate change. The seasonal temperature amplitudes simulated at different depths for the historical period were compared to measured seasonal amplitudes from *in-situ* spring monitoring, and this comparison indicated that the lagoon intertidal springs are sourced from a range of aquifer depths (from 4 m to more than 12 m). The response to seasonal forcing provided qualitative insight into how different springs within the same small lagoon may respond to multi-decadal forcing. Downscaled climate scenarios were used to drive future simulations to 2100, and the results revealed depth-dependent groundwater warming, with warming more pronounced at shallower depths (e.g., ≤ 2.23°C at 4.2 m) and less pronounced at greater depths (≤ 1.62°C warming at 13.9 m). The reduced warming with depth is a result of the depth-dependent lag between surface and groundwater warming signals. To our knowledge, no previous studies have investigated groundwater thermal sensitivity as a driver of future change in coastal lagoon ecosystems. Our results indicate that submarine or intertidal groundwater discharge sourced from shallow aquifers will likely experience non-negligible warming in this century and may strongly influence the shoreline ecosystem where springs are located. The interaction of spring discharge warming with lagoon changes due to sea-level rise and changing atmospheric forcing warrant further consideration and should be considered in future research using coupled thermal and hydrodynamic modelling ~~for the lagoon~~. Future work could more fully integrate paired hydrologic and ecologic studies to better understand how resident species utilise s~~the s~~pring-sourced thermal refuges.

Author contribution

JKA and BK designed the field program, and JKA led the execution of the field program and associated data analysis. AM assisted with radon data collection, and JT led the radon data analysis. JKA led the numerical modelling work with technical support from AM, BK, and SD. BK and RJ led the funding acquisition. BK supervised all aspects of the study. All authors contributed to the study methodology development and manuscript writing.

Competing interests

The authors declare that they have no conflict of interest

Code availability

The SHAW model and associated manuals can be downloaded from the U.S. Department of Agriculture website: https://www.ars.usda.gov/pacific-west-area/boise-id/northwest-watershed-research-center/docs/shaw-model/. Model input files and executables specifically used for this study are archived through a Scholars Portal Dataverse database (see clean version for link). A readme file explains how to run the model for the different climate scenarios.

Data availability

Field data presented in this study and SHAW model input and executable files are ~~temporarily~~ available via a Scholars Portal Dataverse database: ~~https://dataverse.scholarsportal.info/privateurl.xhtml?token=e27331b7-02e5-445b-a190-8ee82c4a4cd2~~(see clean version for link). ~~If accepted, this dataset will be permanently archived with a DOI, and this temporary link will be broken (refer to final paper).~~ A readme file explains each file and how they are connected.

Other supporting tables and figures are provided in the electronic supplement to this paper.

Acknowledgements

Research funding was provided by an NSERC Discovery Grant to B. Kurylyk~~-~~ and the Ocean Frontier Institute (Opportunity Fund program) through an award from the Canada First Research Excellence Fund (CFREF). This study is also a component of an affiliate project with the Global Water Futures CFREF program. Fisheries and Oceans Canada and Souris Fish and Wildlife are thanked for logistical, financial, and/or field support. J. KarisAllen was supported through an NSERC Canada Graduate Scholarship and the NSERC CREATE ASPIRE program. B. Kurylyk and R. Jamieson are supported through the Canada Research Chairs Program. J. Tamborski and A. Mohammed were funded through the Ocean Frontier Institute International Postdoctoral Fellowship Program while at Dalhousie University. We appreciate helpful comments from the Editor and two anonymous reviewers.

References

Abraham, J. P., Baringer, M., Bindoff, N. L., Boyer, T., Cheng, L. J., Church, J. A., Conroy, J. L., Domingues, C. M., Fasullo, J. T., Gilson, J., Goni, G., Good, S. A., Gorman, J. M., Gouretski, V., Ishii, M., Johnson, G. C., Kizu, S., Lyman, J. M., Macdonald, A. M., … Willis, J. K.: A review of global ocean temperature observations: Implications for ocean heat content estimates and climate change. Rev. Geophys., 51, 450–483. https://doi.org/10.1002/rog.20022, 2013.

Anderson, M.: Heat as a groundwater tracer. Groundwater, 43(6), 951-968. https://doi.org/10.1111/j.1745-6584.2005.00052.x, 2005.

Anderson, R. P.: A framework for using niche models to estimate impacts of climate change on species distributions. Annals of the New York Academy of Sciences, 1297, 8–28. https://doi.org/10.1111/nyas.12264, 2013.

Bartlett, G. L.: Quantifying the temporal variability of discharge and nitrate loadings for intertidal springs in two Prince Edward Island estuaries. MSc thesis. University of New Brunswick, New Brunswick, Canada, 2011.

Bejannin, S., van Beek, P., Stieglitz, T., Souhaut, M., & Tamborski, J.: Combining airborne thermal infrared images and radium isotopes to study submarine groundwater discharge along the French Mediterranean coastline. J. Hydrol.: Regional Studies, 13(1), 72–90. https://doi.org/10.1016/j.ejrh.2017.08.001, 2017.

Bense, V. F., & Kurylyk, B. L.: Tracking the subsurface signal of decadal climate warming to quantify vertical groundwater flow rates. Geophys. Res. Lett., 44, 244–253. https://doi.org/10.1002/2017GL076015, 2017.

Benz, S. A., Menberg, K., Bayer, P., & Kurylyk, B. L.: Shallow subsurface heat recycling is a sustainable global space heating alternative. *Nat. Comm.*, 13(3962). https://doi.org/10.1038/s41467-022-31624-6, 2022.

Benson, V. S., VanLeeuwen, J. A., Stryhn, H., & Somers, G. H.: Temporal analysis of groundwater nitrate concentrations from wells in Prince Edward Island, Canada: Application of a linear mixed effects model. Hydrogeo. J., 15(5), 1009–1019. https://doi.org/10.1007/s10040-006-0153-x, 2007.

Bird, N., Chen, L., & McLachlan, J.: Effects of temperature, light and salinity on growth in culture of Chondrus crispus, Furcellaria lumbricalis, Gracilaria tikvahiae (*Gigartinales, Rhodophyta*), and Fucus serratus (*Fucales, Phaeophyta*). Botanica Marina, 22(8), 521–527. https://doi.org/10.1515/botm.1979.22.8.521, 1979.

Bonan, G. B., Ecological Climatology: Concepts and Applications (2nd ed.). Cambridge University Press. https://doi.org/DOI: 10.1017/CBO9780511805530, Cambridge, United Kingdom, 2008.

Brandon, L. V.: Groundwater hydrology and water supply of Prince Edward Island (Paper 64-38). Geological Survey of Canada. https://doi.org/10.4095/101003, 1966.

Briggs, M. A., Johnson, Z. C., Snyder C. D., Hitt, N. P., Kurylyk B. L., Lautz, L., Irvine, D. J., Hurley, S. T., & Lane, J. W.: Inferring watershed hydraulics and cold-water habitat persistence using multi-year air and stream temperature signals. Sci. Tot. Environ., 636, 1117-1127. https://doi.org/10.1016/j.scitotenv.2018.04.344, 2018a.

Briggs, M. A., Lane, J. W., Snyder, C. D., White, E. A., Johnson, Z. C., Nelms, D. L, Hitt, N. P.: Shallow bedrock limits groundwater seepage-based headwater climate refugia. Limnologica 68, 142-156. https://doi.org/10.1016/j.limno.2017.02.005, 2018b.

Brookfield, A. E., Sudicky, E. A., Park, Y.-J., & Conant Jr., B.:Thermal transport modelling in a fully integrated surface/subsurface framework. Hydrol. Process., 23(15), 2150–2164. https://doi.org/10.1002/hyp.7282, 2009.

Burnett, W. C., & Dulaiova, H.: Estimating the dynamics of groundwater input into the coastal zone via continuous radon-222 measurements. J. Environ. Rad., 69(1), 21–35. https://doi.org/10.1016/S0265-931X(03)00084-5, 2003.

Cantonati, M., Stevens, L. E., Segadelli, S., Springer, A. E., Goldscheider, N., Celico, F., Filippini,M., Ogata, K., Gargini, A.: Ecohydrogeology: The interdisciplinary convergence needed to improve the study and stewardship of springs and other groundwater-dependent habitats, biota, and ecosystems. Ecol. Indic., 10, 105802. https://doi.org/10.1016/j.ecolind.2019.105803, 2020.

Caissie, D.: The thermal regime of rivers: A review. Freshwater Biol., 51(8), 1389–1406. https://doi.org/10.1111/j.1365-2427.2006.01597.x, 2006.

Chikita, K. A., Uyehara, H., Mamun, A. Al, Umgiesser, G., Iwasaka, W., Hossain, M. M., & Sakata, Y.: Water and heat budgets in a coastal lagoon controlled by groundwater outflow to the ocean. Limnology, 16(3), 149–157. https://doi.org/10.1007/s10201-015-0449-4, 2015.

Coluccio, K., Santos, I., Jeffrey, L. C., Katurji, M., Coluccio, S., & Morgan, L. K.: Mapping groundwater discharge to a coastal lagoon using combined spatial airborne thermal imaging, radon (222Rn) and multiple physicochemical variables. Hydrol. Process., 34(24), 4592–4608. https://doi.org/10.1002/hyp.13903, 2020.

Crowl, G. H.: Geology of Mount Stewart-Souris map-area, Prince Edward Island (11 L/7, L/8) (Paper 67-66). Geological Survey of Canada. https://doi.org/10.4095/102347, 1969a.

Crowl, G. H.: Surficial geology, Mount Stewart - Souris, Prince Edward Island ["A" Series Map 1260A] (Paper 67-66). Geological Survey of Canada. https://doi.org/10.4095/108918, 1969b.

Danielescu, S., MacQuarrie, K. T. B., & Faux, R.: The integration of thermal infrared imaging, discharge measurements and numerical simulation to quantify the relative contributions of freshwater inflows to small estuaries in Atlantic Canada. Hydrol. Process., 23(20), 2847–2859. https://doi.org/10.1002/hyp.7383, 2009.

Desbruyères, D., McDonagh, E. L., King, B. A., & Thierry, V.: Global and full-depth ocean temperature trends during the early twenty-first century from Argo and repeat hydrography. J. Clim., 30(6), 1985–1997. https://doi.org/10.1175/JCLI-D-16-0396.1, 2017.

DeVries, D. A.: Thermal properties of soils, in: Physics of Plant Evironment, edited by W. R. Van Wijk (Ed.), (p. 382). North-Holland Publishing Co., 1963.

DFO: Ecological assessment of Irish moss (*Chondrus crispus*) in Basin Head Marine Protected Area [corrected August 2011] (Gulf Region CSAS Science Advisory Report 2008/059). Fisheries and Oceans Canada, Moncton, Canada, 2009.

Dignman, S. L.: Physical Hydrology (2nd edition). Long Grove, Illinois, Waveland Press, 2002.

DJI: Zenmuse XT 2 - User manual V1.0. https://dl.djicdn.com/downloads/Zenmuse XT 2/Zenmuse XT 2 User Manual v1.0_.pdf, 2018.

Dowd, W. W., & Somero, G. N.: Behavior and survival of *Mytilus congeners* following episodes of elevated body temperature in air and seawater. J. Exper. Biol., 216, 502–514. https://doi.org/10.1242/jeb.076620, 2003.

Dugdale S. J., Hannah, D. M., & Malcolm, I. A.: River temperature modelling: A review of process-based approaches and future directions. Earth Sci. Rev., 175, 97-113. https://doi.org/10.1016/j.earscirev.2017.10.009, 2017.

Dugdale, S. J., Kelleher, C. A., Malcolm, I. A., Caldwell, S., & Hannah, D. M.: Assessing the potential of drone-based thermal infrared imagery for quantifying river temperature heterogeneity. Hydrol. Process., 33, 1152–1163. https://doi.org/10.1002/hyp.13395, 2019.

Dugdale S. J., Klaus, J, & Hannah, D. M.: Looking to the skies: realising the combined potential of drones and thermal infrared imagery to advance hydrological process understanding in headwaters. Wat. Resour. Res., e2021WR031168, https://doi.org/10.1029/2021WR031168.

ECCC (Environment and Climate Change Canada). 2021a. Hourly data report, East Point Weather Station (Climate ID 8300418), Prince Edward Island. Accessed at: https://climate.weather.gc.ca/climate_data/hourly_data_e.html?hlyRange=1994-02-01%7C2022-01-02&dlyRange=1992-12-08%7C2022-01-02&mlyRange=2004-01-01%7C2007-07-01&StationID=7177&Prov=PE&urlExtension=_e.html&searchType=stnName&optLimit=yearRange&StartYear=1840&EndYear=2022&selRowPerPage=25&Line=0&searchMethod=contains&Month=1&Day=2&txtStationName=east+point&timeframe=1&Year=2022

ECCC (Environment and Climate Change Canada). 2021b. Hourly data report, St. Peters Weather Station (Climate ID 8300562), Prince Edward Island. Accessed at: https://climate.weather.gc.ca/climate_data/hourly_data_e.html?hlyRange=2003-08-14%7C2022-01-01&dlyRange=2003-08-14%7C2022-01-01&mlyRange=2004-01-01%7C2007-07-01&StationID=41903&Prov=PE&urlExtension=_e.html&searchType=stnName&optLimit=yearRange&StartYear=1840&EndYear=2022&selRowPerPage=25&Line=0&searchMethod=contains&Month=1&Day=1&txtStationName=st+peter&timeframe=1&Year=2022

Environment and Climate Change Canada (ECCC), Computer Research Institute of Montréal (CRIM), Ouranos, the Pacific Climate Impacts Consortium (PCIC), the Prairie Climate Centre (PCC), & HabitatSeven: Climate data for a resilient Canada. https://climatedata.ca/, 2021.

Flerchinger, G.: The simultaneous heat and water (SHAW) model: Technical documentation (version 3.0) (Technical Report NWRC 2000-09). USDA Agricultural Research Service. https://www.ars.usda.gov/ARSUserFiles/20520000/shawdocumentation.pdf, 2017.

Flerchinger, G., & Saxton, K.: Simultaneous Heat and Water Model of a freezing snow-residue-soil system I. Theory and development. Trans. ASAE, 32, 565–571. https://doi.org/10.13031/2013.31040, 1989.

Gilfedder, B. S., Frei, S., Hofmann, H., & Cartwright, I.: Groundwater discharge to wetlands driven by storm and flood events: Quantification using continuous Radon-222 and electrical conductivity measurements and dynamic mass-balance modelling. Geochimica et Cosmochimica Acta, 165, 161–177. https://doi.org/10.1016/j.gca.2015.05.037, 2015.

Government of PEI: Water well information system [Kingsboro well logs from 1974 to 2012], 2019.

Government of PEI: Ground water data: Observation well data [Souris Line Road]. http://www.gov.pe.ca/envengfor/groundwater/app.php?map=YES&id=SL&lang=E, 2021

Graf, T., & Therrien, R.: Coupled thermohaline groundwater flow and single-species reactive solute transport in fractured porous media. Adv. Wat. Res., 30(4), 742–771. https://doi.org/10.1016/j.advwatres.2006.07.001, 2007.

Grzelak, K., Tamborski, J., Lotwicki, L., & Bokuniewicz, H.: Ecostructuring of marine nematode communities by submarine groundwater discharge. Marine Environ. Res., 136, 106-119. https://doi.org/10.1016/j.marenvres.2018.01.013, 2008.

Gunawardhana, L. N., & Kazama, S.: Climate change impacts on groundwater temperature change in the Sendai plain, Japan. Hydrol. Process., 25(17), 2665–2678. https://doi.org/10.1002/hyp.8008, 2011.

Gunawardhana L. N., Kazama, S., & Kawagoe, S.: Impact of urbanization and climate change on aquifer thermal regimes. Water Resour. Manage., 25, 3247-3276, 2011. https://doi.org/10.1007/s11269-011-9854-6.

Hannah, D. M., & Garner, G.: River water temperature in the United Kingdom: Changes over the 20th century and possible changes over the 21st century. Prog. Phys. Geog.: Earth Environ., 39(1), 68–92. https://doi.org/10.1177/0309133314550669, 2015.

Hayashi, M. & Rosenberry, D. O.: Effects of ground water exchange on the hydrology and ecology of surface water. Ground Water, 40(3), 309-216. https://doi.org/10.1111/j.1745-6584.2002.tb02659.x, 2002.

IPCC: Climate change 2014 Synthesis Report - Contribution of working groups I, II and III to the fifth Assessment Report of the Intergovernmental Panel on Climate Change [Core writing team, Pachauri, R.K. and Meyer, L.A. (eds.)], 2014.

Isaak, D. J., Wenger, S. J., Peterson, E. E., Ver Hoef, J. M., Nagel, D. E., Luce, C. H., Hostetler, S. W., Dunham, J. B., Roper, B. B., Wollrab, S. P., Chandler, G. L., Horan, D. L., & Parkes-Payne, S.: The NorWeST summer stream temperature model and scenarios for the western U.S.: A crowd-sourced database and new geospatial tools foster a user community and predict broad climate warming of rivers and streams. Wat. Resour. Res., 53(11), 9181–9205. https://doi.org/10.1016/j.scitotenv.2016.08.212, 2017.

Irvine, D. J., Kurylyk, B. L., Cartwright, I., Bonham, M., Post, V. E. A., Banks, E. W., Simmons, C. T.: Groundwater flow estimation using temperature-depth profiles in a complex environment and a changing climate. Sci. Tot. Environ. 574, 272-281, 2017. https://doi.org/

Ji, Z.-G.: Hydrodynamics, in: Hydrodynamics and Water Quality: Modelling Rivers, Lakes, and Estuaries (2nd ed., pp. 11–71). John Wiley & Sons Inc. https://doi.org/10.1002/9780470241066.ch2, 2017.

Johnson, Z. C., Johnson B. G., Briggs, M. A., Devine, W. D., Snyder, C. D., Hitt, N. P., Hare, D. K. & Minkova T. V.: Paired air-water annual temperature patterns reveal hydrogeological controls on stream thermal regimes at watershed to continental scales. J. Hydrol., 587, 124929. https://doi.org/10.1016/j.jhydrol.2020.124929, 2020.

Joseph, V., Thériault, M.-H., Novaczek, I., Coffin, M., Cairns, D., Nadeau, A., Boudreau, M., Plourde, M.-A., Quijon, P. A., & Tummon Flynn, P.: Review of monitoring activities in the Basin Head Marine Protected Area in the context of their effectiveness in evaluating attainment of conservation objectives (Canadian Science Advisory Secretariat Research Document 2021/044). Fisheries and Oceans Canada, Moncton, Canada. https://www.dfo-mpo.gc.ca/csas-sccs/Publications/ResDocs-DocRech/2021/2021_044-eng.pdf, 2021.

Kaandorp, V. P., Doornenbal, P. J., Kooi, H., Peter Broers, H., & de Louw, P. G. B.: Temperature buffering by groundwater in ecologically valuable lowland streams under current and future climate conditions. J. Hydrol. X, 3, 100031, 2019.

Kalacska, M., Lucanus, O., Arroyo-Mora, J. P., Laliberté, É., Elmer, K., Leblanc, G., & Groves, A.: Accuracy of 3D landscape reconstruction without ground control points using different UAS platforms. Drones, 4(2), 13. https://doi.org/10.3390/drones4020013, 2020.

Kang, K., Kim, D., Kim, Y., Lee, E., Kim, B.-G., Kim, S. H., Ha, K., Koh, D.-C., Cho, Y.-K., & Kim, G. Quantitative estimation of submarine groundwater discharge using airborne thermal infrared data acquired at two different tidal heights. Hydrol. Process., 33(7), 1089–1100. https://doi.org/10.1002/hyp.13387, 2019.

KarisAllen, J. J., & Kurylyk, B. L.: Drone-based characterization of intertidal spring cold-water plume dynamics. Hydrol. Process., 35(6), e14258. https://doi.org/10.1002/hyp.14258, 2021.

Kelleher, C., Wagener, T., Gooseff, M., McGlynn, B., McGuire, K. & Marshall, L.: Investigating controls on the thermal sensitivity of Pennsylvania streams. Hydrol. Process., 26(5), 771-785. https://doi.org/10.1002/hyp.8186, 2012.

Kelly, J., Kljun, N., Olsson, P.-O., Mihai, L., Liljeblad, B., Weslien, P., Klemedtsson, L., & Eklundh, L.: Challenges and best practices for deriving temperature data from an uncalibrated UAV thermal infrared camera. Remote Sensing, 11. https://doi.org/10.3390/rs11050567, 2019a.

Kelly, J. L., Dulai, H., Glenn, C. R., & Lucey, P. G. Integration of aerial infrared thermography and in situ radon-222 to investigate submarine groundwater discharge to Pearl Harbor, Hawaii, USA. Limnol. Ocean, 64(1). https://doi.org/10.1002/lno.11033, 2019b.

Kübler, J. E., & Davison, I. R.: High-temperature tolerance of photosynthesis in the red alga *Chondrus crispus*. Marine Biol., 117(2), 327–335. https://doi.org/10.1007/BF00345678, 1993.

Kurylyk, B. L., MacQuarrie, K. T. B., Linnansaari, T., Cunjak, R. A., & Curry, R. A.: Preserving, augmenting, and creating cold-water thermal refugia in rivers: concepts derived from research on the Miramichi River, New Brunswick (Canada). Ecohydrology, 8(6), 1095–1108. https://doi.org/10.1002/eco.1566, 2015a.

Kurylyk, B. L., MacQuarrie, K. T. B., Caissie, D., & McKenzie, J. M.: Shallow groundwater thermal sensitivity to climate change and land cover disturbances: Derivation of analytical expressions and implications for stream temperature modeling. Hydrol. Earth Syst. Sci., 19, 2469–2489. https://doi.org/10.5194/hess-19-2469-2015, 2015b.

Kurylyk, B. L., MacQuarrie, K. T. B., & McKenzie, J. M.: Climate change impacts on groundwater and soil temperatures in cold and temperate regions: Implications, mathematical theory, and emerging simulation tools. Earth-Sci. Rev., 138, 313–334. https://doi.org/10.1016/j.earscirev.2014.06.006, 2014a.

Kurylyk, B. L., MacQuarrie, K. T. B., & Voss, C. I.: Climate change impacts on the temperature and magnitude of groundwater discharge from shallow, unconfined aquifers. Wat. Resour. Res., 50(4), 3253–3274. https://doi.org/10.1002/2013WR014588, 2014b.

Kurylyk, B. L., Moore, R. D., & MacQuarrie, K. T. B.: Scientific briefing: Quantifying streambed heat advection associated with groundwater–surface water interactions. Hydrol. Process., 30(6), 987–992. https://doi.org/10.1002/hyp.10709, 2016.

Langford, J.E., Schincariol, R.A., Nagare, R.M., Quinton, W.L., & Mohammed, A.A.: Transient and transition factors in modeling permafrost thaw and groundwater flow. Groundwater, 58(2), 258-268. https://doi: 10.1111/gwat.12903, 2020.

Lecher, A. L, & Mackey, R. M.: Synthesizing the effects of submarine groundwater discharge on marine biota. Hydrology, 54(4). https://doi.org/10.3390/hydrology5040060.

Lee, E., Kang, K., Hyun, S. P., Lee, K.-Y., Yoon, H., Kim, S. H., Kim, Y., Xu, Z., Kim, D., Koh, D.-C., & Ha, K.: Submarine groundwater discharge revealed by aerial thermal infrared imagery: a case study on Jeju Island, Korea. Hydrol. Process., 30(19), 3494–3506. https://doi.org/10.1002/hyp.10868, 2016a.

Lee, E., Yoon, H., Hyun, S. P., Burnett, W. C., Koh, D.-C., Ha, K., Kim, D., Kim, Y., & Kang, K.: Unmanned aerial vehicles (UAVs)-based thermal infrared (TIR) mapping, a novel approach to assess groundwater discharge into the coastal zone. Limnol. Ocean.: Methods, 14(11), 725–735. https://doi.org/10.1002/lom3.10132kurl, 2016b.

LeRoux, N. K., Kurylyk, B. L., Briggs, M. A., Irvine, D. J., Tamborski, J. J., & Bense, V. F.: Using heat to trace vertical water fluxes in sediment experiencing concurrent tidal pumping and groundwater discharge. Wat. Resour. Res., 57(2), e2020WR027904. https://doi.org/10.1029/2020WR027904, 2021.

Liu, S., Xie, Z., Liu, B., Wang, Y., Gao, J., Zeng, Y., Xie, J., Xie, Z., Jia, B., Qin, P., Li, R., Wang, L., & Chen, S.: Global river water warming due to climate change and anthropogenic heat emission. Global and Planetary Change, 193, 103289. https://doi.org/10.1016/j.gloplacha.2020.103289, 2020.

Luijendijk, E., Gleeson, T., & Moosdorf, N.: Fresh groundwater discharge insignificant for the world's oceans but important for coastal ecosystems. Nat. Comm., 11(1), 1260. https://doi.org/10.1038/s41467-020-15064-8, 2020.

Lüning, K., Guiry, M. D., & Masuda, M.: Upper temperature tolerance of North Atlantic and North Pacific geographical isolates of Chondrus species (*Rhodophyta*). Helgoländer Meeresuntersuchungen, 41(3), 297–306. https://doi.org/10.1007/BF02366194, 1986.

MacIntyre, S., Wanninkhof, R., & Chanto, J. P.: Trace gas exchange across the air-water interface in freshwater and coastal marine environments, in: Biogenic Trace Gases: Measuring Emissions from Soil and Water (pp. 52–97), edited by P. A. Matson & R. C. Harris (Eds.). Blackwell Science, 1995.

Mathieson, A. C., & Burns, R. L.: Ecological studies of economic red algae. I. Photosynthesis and respiration of *Chondrus crispus* Stackhouse and *Gigartina stellata* (stackhouse) batters. J. Exper. Marine Biol. Ecol., 7(2), 197–206. https://doi.org/10.1016/0022-0981(71)90031-1, 1971.

Mayer, T. D.: Controls of summer stream temperature in the Pacific Northwest. J. Hydro., 475, 323-335, https://doi.org/10.1016/j.jhydrol.2012.10.012, 2012.

Menberg, K., Blum, P., Kurylyk, B. L., & Bayer, P.: Observed groundwater temperature response to recent climate change. Hydrol. Earth Syst. Sci., 18(11), 4453–4466. https://doi.org/10.5194/hess-18-4453-2014, 2014.

Mohammed, A. A., Schincariol, R. A., Quinton, W. L., Nagare, R. M., & Flerchinger, G.: On the use of mulching to mitigate permafrost thaw due to linear disturbances in sub-arctic peatlands. Ecol. Eng., 102, 207–223. https://doi.org/10.1016/j.ecoleng.2017.02.020, 2017.

Morash, A. J., Speers-Roesch, B., Andrew, S., & Currie, S.: The physiological ups and downs of thermal variability in temperate freshwater ecosystems. J. Fish Biol. 98(6), 1524–1535. https://doi.org/10.1111/jfb.14655, 2021.

Mundy, E., Gleeson, T., Roberts, M., Baraer, M., & McKenzie, J. M.: Thermal imagery of groundwater seeps: possibilities and limitations. Groundwater, 55(2), 160–170. https://doi.org/10.1111/gwat.12451, 2017.

Newton, A., & Mudge, S. M.: Temperature and salinity regimes in a shallow, mesotidal lagoon, the Ria Formosa, Portugal. Estuarine, Coastal and Shelf Science, 57(1), 73–85. https://doi.org/10.1016/S0272-7714(02)00332-3, 2003.

Nunes, R. A., & Lennon, G. W.: Episodic stratification and gravity currents in a marine environment of modulated turbulence. J. Geophys. Res.: Oceans, 92(C5), 5465–5480. https://doi.org/10.1029/JC092iC05p05465, 1987.

O'Sullivan, A. M., Devito, K. J., & Curry, R. A.: The influence of landscape characteristics on the spatial variability of river temperatures. Catena, 177, 70-93, http://doi.org/ 10.1016/j.catena.2019.02.006, 2019.

Ouellet, V., St-Hilaire, A., Dugdale, S. J., Hannah, D. M., Krause, S., & Proulx-Ouellet, S.: River temperature research and practice: Recent challenges and emerging opportunities for managing thermal habitat conditions in stream ecosystems. Sci. Tot. Environment, 736, 139679. https://doi.org/10.1016/j.scitotenv.2020.139679, 2020.

Peterson, R. N., Santos, I. R., & Burnett, W. C.: Evaluating groundwater discharge to tidal rivers based on a Rn-222 time-series approach. Estuarine, Coastal and Shelf Science, 86(2), 165–178. https://doi.org/10.1016/j.ecss.2009.10.022, 2010.

Prest, V. K.: Surficial deposits of Prince Edward Island ["A" Series Map 1366A]. Geological Survey of Canada, 1973.

Rodellas, V., Stieglitz, T. C., Tamborski, J. J., van Beek, P., Andrisoa, A., & Cook, P. G.: Conceptual uncertainties in groundwater and porewater fluxes estimated by radon and radium mass balances. Limnol. Ocean., 66(4), 1237–1255. https://doi.org/10.1002/lno.11678, 2021.

Rodríguez-Rodríguez, M., & Moreno-Ostos, E.: Heat budget, energy storage and hydrological regime in a coastal lagoon. Limnologica, 36(4), 217–227. https://doi.org/10.1016/j.limno.2006.05.003, 2006.

Roseen, R. M.: Quantifying groundwater discharge using thermal imagery and conventional groundwater exploration techniques for estimating the nitrogen loading to a meso-scale estuary, Doctoral dissertation, University of New Hampshire, New Hampshire, United States. https://scholars.unh.edu/dissertation/77, 2002.

Sadat-Noori, M., Santos, I. R., Sanders, C. J., Sanders, L. M., & Maher, D. T.: Groundwater discharge into an estuary using spatially distributed radon time series and radium isotopes. J. Hydrol., 528, 703–719. https://doi.org/10.1016/j.jhydrol.2015.06.056, 2015.

Schubert, M., Paschke, A., Lieberman, E., & Burnett, W. C.: Air–Water partitioning of 222Rn and its dependence on water temperature and salinity. Environ. Sci. Technol., 46(7), 3905–3911. https://doi.org/10.1021/es204680n, 2012.

Sparks, A.: Nasapower: A NASA POWER global meteorology, surface solar energy and climatology data client for R. Journal of Open Source Software, 3(30), 1035. https://doi.org/10.21105/joss.01035, 2018.

Stallman, R. W.: Steady one-dimensional fluid flow in a semi-infinite porous medium with sinusoidal surface temperature. J. Geophys. Res., 70, 2821-2827. https://doi.org/ 10.1029/JZ070i012p02821, 1965

Sullivan, C. J., Vokoun, J. C., Helton, A. M., Briggs, M. A., & Kurylyk, B. L.: An ecohydrological typology for thermal refuges in streams and rivers. Ecohydrology, 14(5), e2295. https://doi.org/10.1002/eco.2295, 2021.

Swarzenski, P. W.: U/Th series radionuclides as coastal groundwater tracers. Chem. Rev., 107(2), 663–674. https://doi.org/10.1021/cr0503761, 2007.

Tamborski, J. J., Rogers, A. D., Bokuniewicz, H. J., Cochran, J. K., & Young, C. R.: Identification and quantification of diffuse fresh submarine groundwater discharge via airborne thermal infrared remote sensing. Rem. Sens. Environ., 171(15), 202–217. https://doi.org/10.1016/j.rse.2015.10.010, 2015.

Tasende, M. A., & Fraga, M. I.: Efecto de las condiciones de cultivo en la germinación de esporas de Chondrus crispus stackh, (Gigartinales, Rhodophyta). Cahiers de Biologie Marine, 33(4), 407–415, 1992.

Torgersen, C. E., Ebersole, J. L., & Keenan, D. M.: Primer for identifying cold-water refuges to protect and restore thermal diversity in riverine landscapes. U.S. Geological Survey. http://pubs.er.usgs.gov/publication/70037945, 2012

van de Poll, H. W.: Lithostratigraphy of the Prince Edward Island redbeds. Atlantic Geology, 25, 23–35. https://doi.org/10.4138/1668, 1989

Voldoire, A., Sanchez-Gomez, E., Mélia, D., Decharme, B., Cassou, C., Senesi, S., Valcke, S., Beau, I., Alias, A., Chevallier, M., Déqué, M., Deshayes, J., Douville, H., Fernandez, E., Madec, G., Maisonnave, E., Moine, M.-P., Planton, S., Saint-Martin, D., & Chauvin, F.: The CNRM-CM5.1 global climate model: Description and basic evaluation. Clim. Dyn., 40, 2091–2121. https://doi.org/10.1007/s00382-011-1259-y, 2013.

Warner, S.: Assessing the potential impact of climate change on the surface hydrology of Prince Edward Island, MASc thesis, Dalhousie University, Halifax, Canada. http://hdl.handle.net/10222/72317, 2016

Wells, M. L., Karlson, B., Wulff, A., Kudela, R., Trick, C., Asnaghi, V., Berdalet, E., Cochlan, W., Davidson, K., De Rijcke, M., Dutkiewicz, S., Hallegraeff, G., Flynn, K. J., Legrand, C., Paerl, H., Silke, J., Suikkanen, S., Thompson, P., & Trainer, V. L.: Future HAB science: Directions and challenges in a changing climate. Harmful Algae, 91, 101632. https://doi.org/10.1016/j.hal.2019.101632, 2020

Wilbur, N. M., O'Sullivan, A. M., MacQuarrie, K. T. B., Linnansaari, T., & Curry, R.A.: Characterizing physical habitat preferences and thermal refuge occupancy of brook trout (*Salvelinus fontinalis*) and Atlantic salmon (*Salmo salar*) at high river temperatures. River Res Applic., 36, 769– 783, 2020. https://doi.org/10.1002/rra.3570

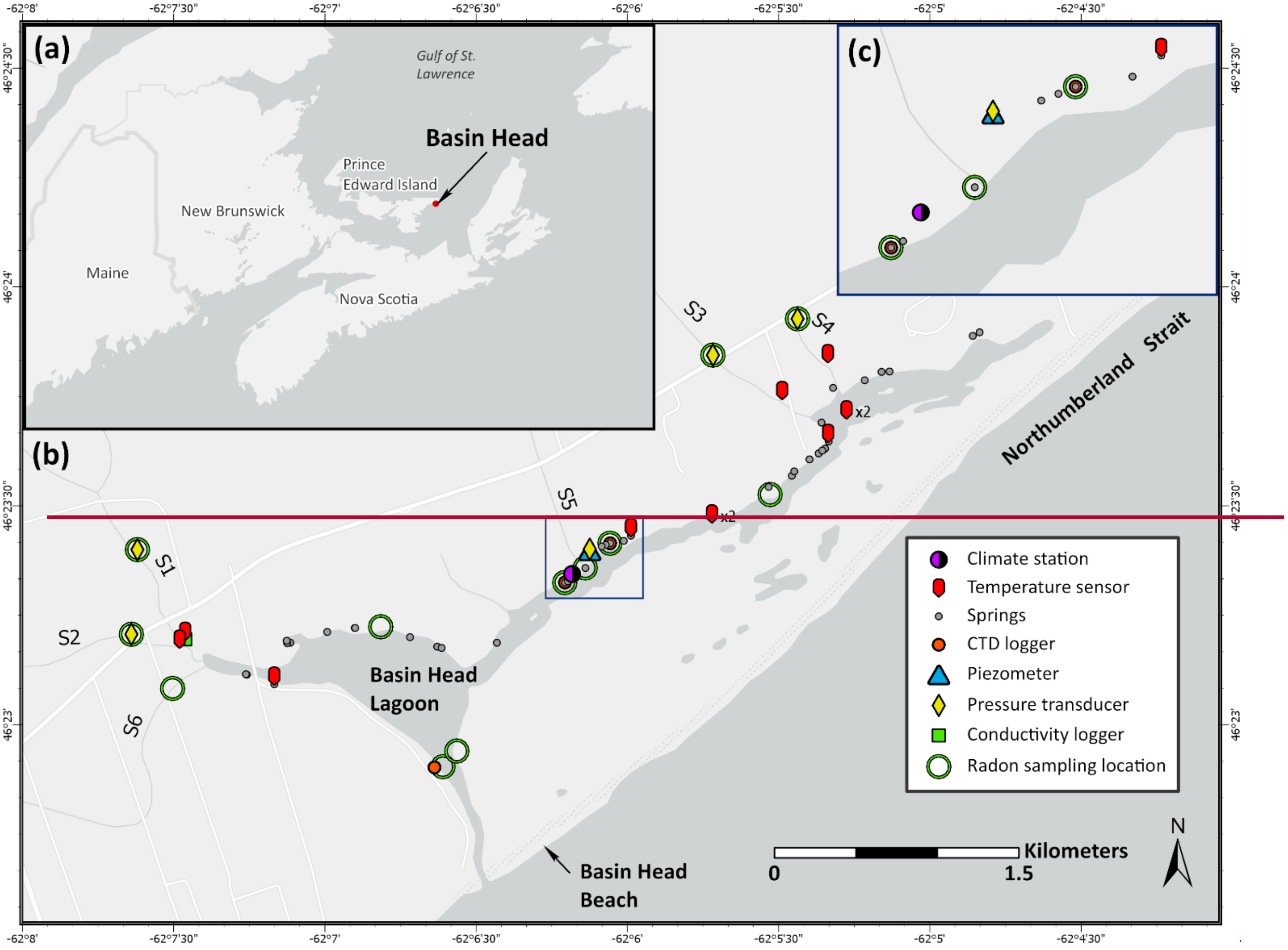
-62°8'
-62°7'30"
-62°7'
-62°6'30"
-62°6'
-62°5'30"
-62°5'
-62°4'30"
46°24'30"
46°24'
46°23'30"
46°23'
(a)
Gulf of St. Lawrence
Basin Head
Prince Edward Island
New Brunswick
Maine
Nova Scotia
(b)
(c)
S1
S2
S3
S4
S5
S6
x2
x2
Basin Head Lagoon
Basin Head Beach
Northumberland Strait
Climate station
Temperature sensor
Springs
CTD logger
Piezometer
Pressure transducer
Conductivity logger
Radon sampling location
0
1.5
Kilometers
N

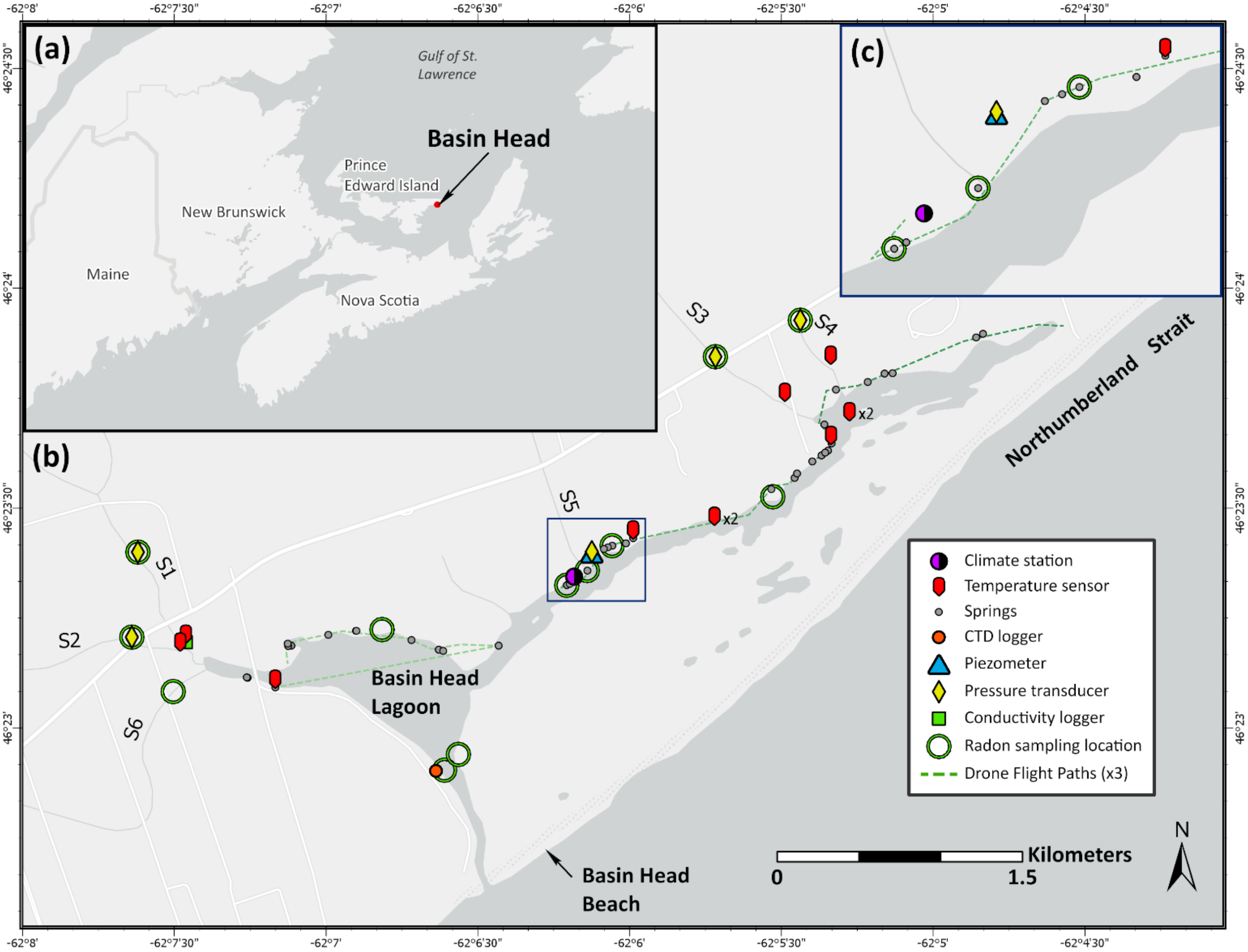

Figure 1: (a) Location of Basin Head lagoon within Atlantic Canada. (b) Instrument, radon sampling, and identified spring locations within Basin Head lagoon and watershed over the duration of the study. Temperature sensors installed in the northeast arm of the lagoon channel were in pairs (labelled as '×2'): one at the top (affixed to a buoy) and bottom (affixed to an anchor) of the water column. Drone surveying was performed in three flights (green dashed line) after scouting surveys had identified spring locations. (c) Enlarged view of the densely instrumented area designated by the blue box in (b). CTD = conductivity, temperature, depth. Basemap is attributed to Esri, HERE, Garmin, FAO, NOAA, USGS, © OpenStreetMap contributors, and the GIS User Community.

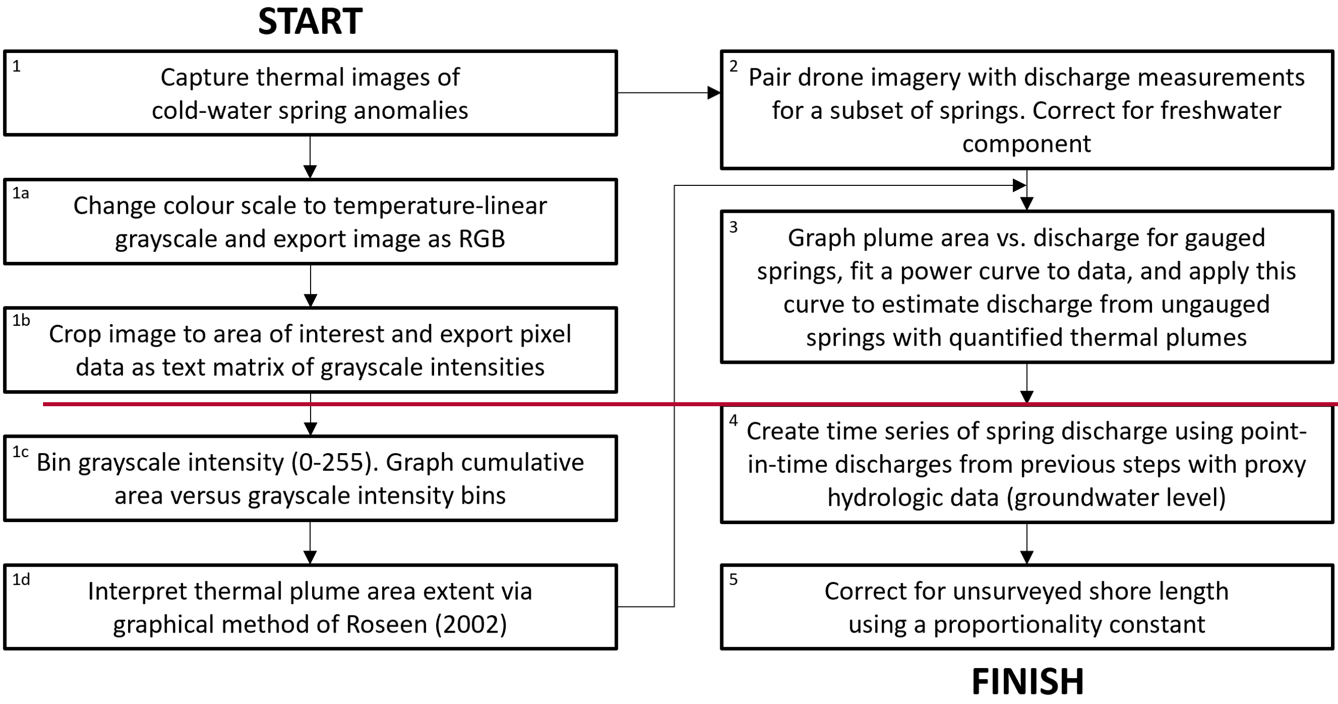
START
1 Capture thermal images of cold-water spring anomalies
1a Change colour scale to temperature-linear grayscale and export image as RGB
1b Crop image to area of interest and export pixel data as text matrix of grayscale intensities
1c Bin grayscale intensity (0-255). Graph cumulative area versus grayscale intensity bins
1d Interpret thermal plume area extent via graphical method of Roseen (2002)
2 Pair drone imagery with discharge measurements for a subset of springs. Correct for freshwater component
3 Graph plume area vs. discharge for gauged springs, fit a power curve to data, and apply this curve to estimate discharge from ungauged springs with quantified thermal plumes
4 Create time series of spring discharge using point-in-time discharges from previous steps with proxy hydrologic data (groundwater level)
5 Correct for unsurveyed shore length using a proportionality constant
FINISH

~~Figure 2: Summary workflow of the spring discharge assessment technique applied in Basin Head lagoon using thermal imagery. Panels a, b, c, and d of Fig. 5 correspond with box numbers 1, 1b, 1c, and 3, respectively.~~

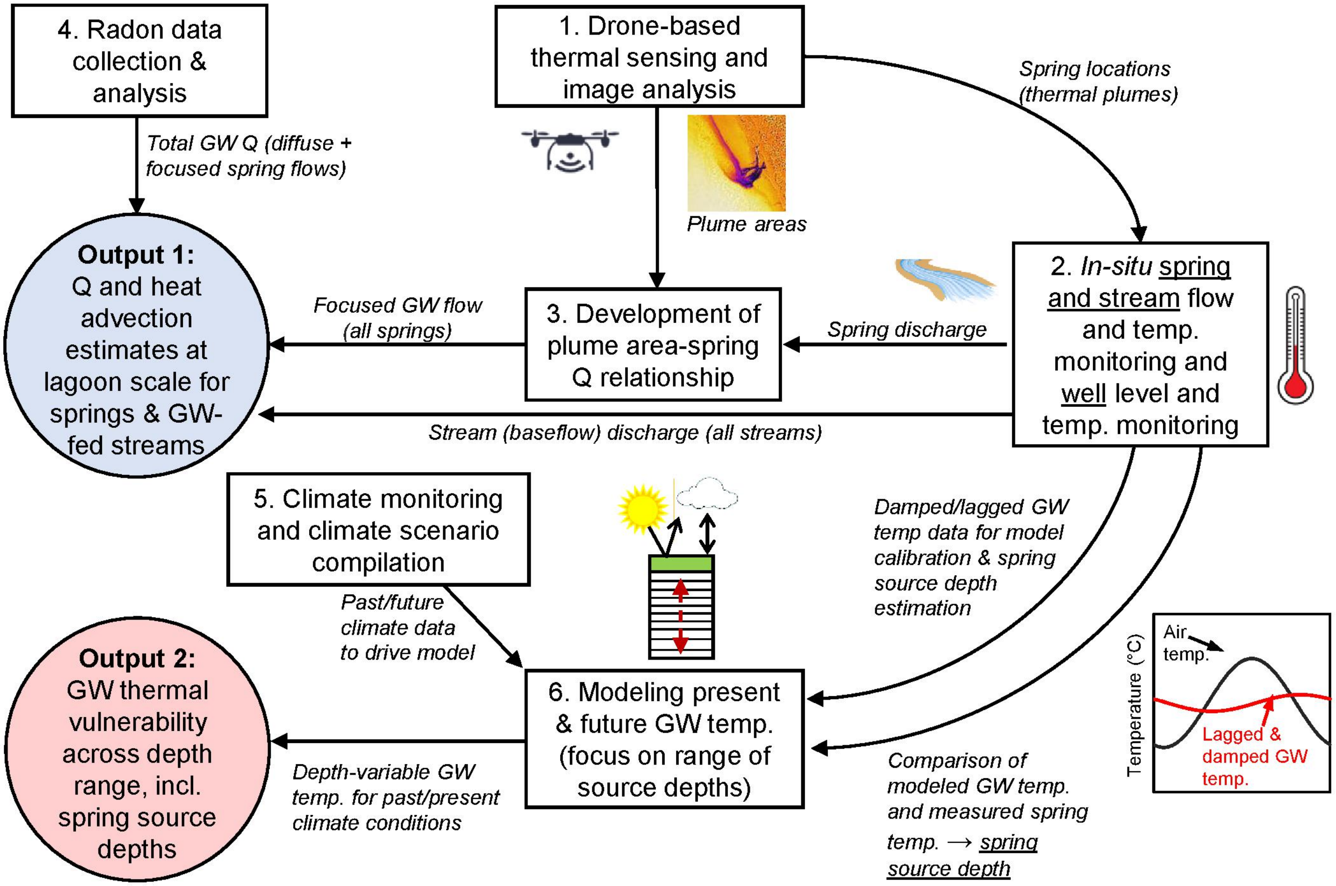

Figure 2: Diagram showing how the different aspects of this study are interrelated. Boxes indicate key study methods/elements, circles indicate key study outputs, and arrows and italicized text indicate outputs from one study element that become inputs for another. Q = discharge; GW = groundwater.

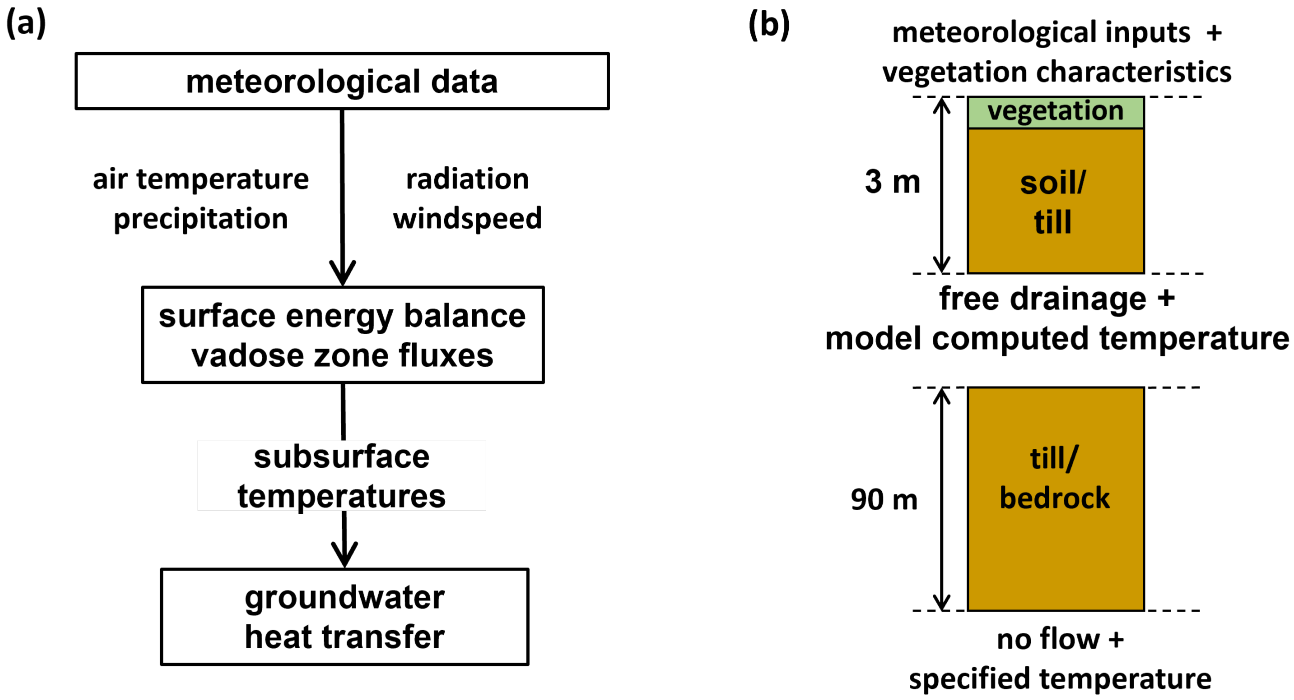

955 **Figure 3: (a) Flowchart showing the conceptualisation of the modeling approach used in this study and (b) conceptual diagram of SHAW model set-up and boundary conditions (not drawn to scale).**

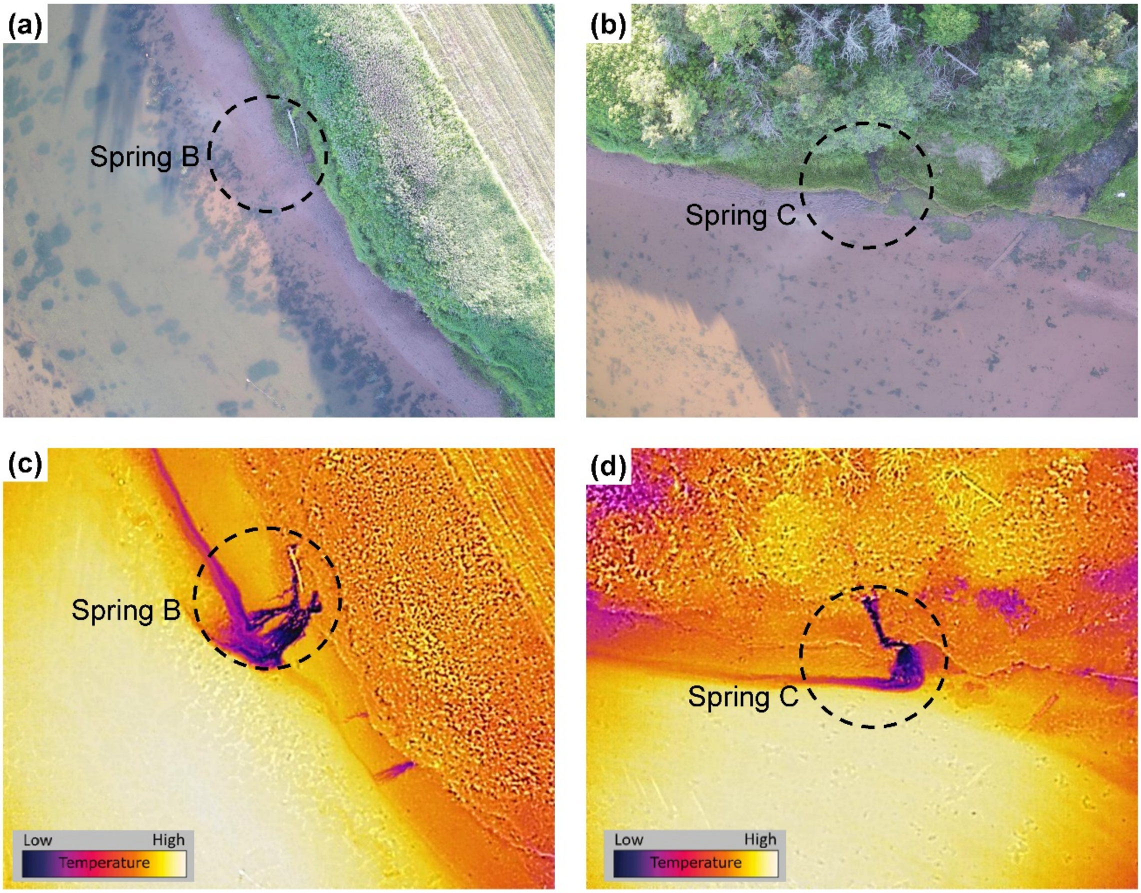

Figure 4: Top row [(a) and (b)], visual drone images of two of the springs that were manually gauged (Springs B and C, see Table S2). Bottom row [(c) and (~~c~~d)]: corresponding thermal images from the drone's thermal sensor. Scales are not equal among panels: there was a maximum thermal offset of 16°C and 12 °C between the spring water and receiving environment for (c) and (d), respectively. Pixel resolutions were 6.0 and 5.2 cm/pixel for panels (c) and (d), respectively.

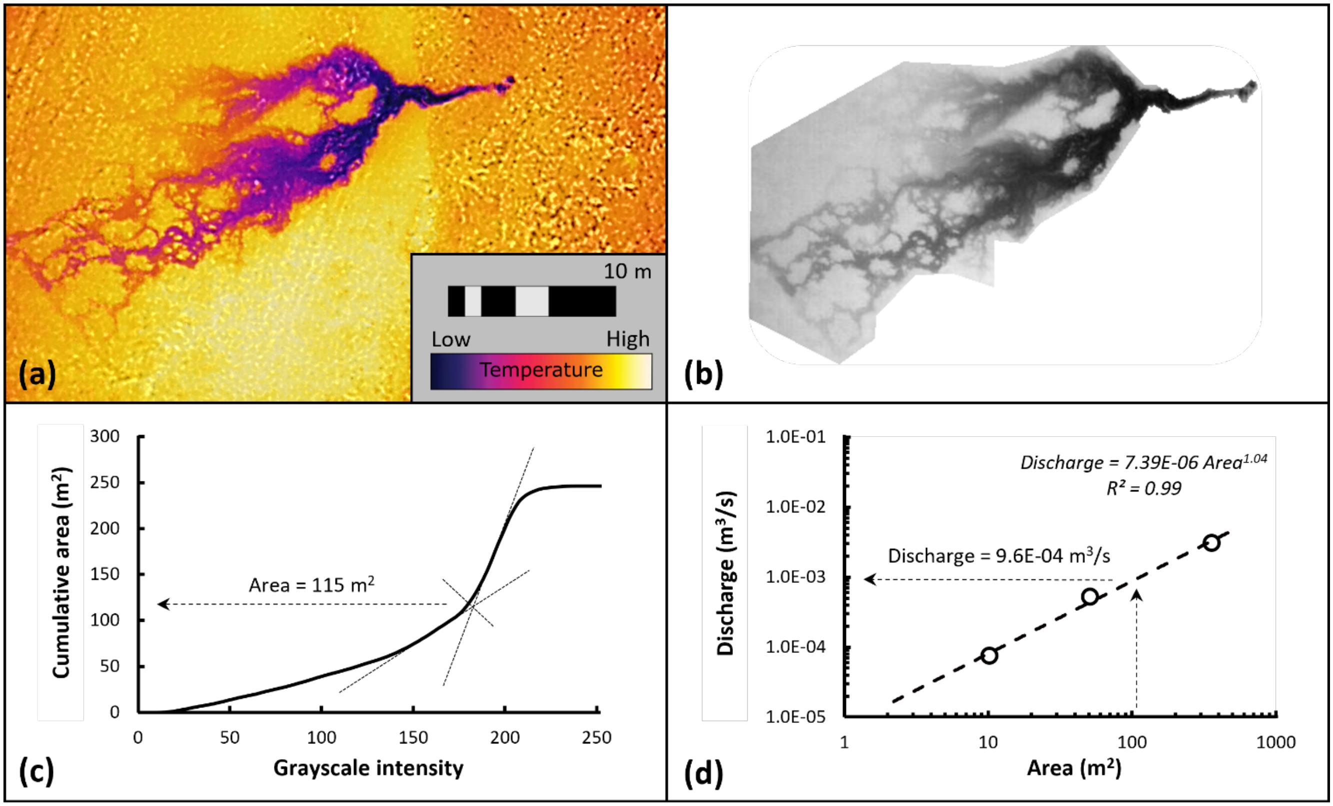

Figure 5: Simplified workflow and results describing the area and discharge analyses of Spring 8 (included in Table S2 and Fig. ~~S4~~S6) using the Basin Head plume size-spring discharge relationship. (a) Raw thermal image of Spring 8 cropped (rectangular) to the spring area (maximum offset of 14°C between the spring water and discharge environment; pixel resolution of 6 cm/pixel). (b) Thermal image converted to 8-bit grayscale and cropped (polygonal) to thermal groups of interest. (c) Graph of thermal image pixel data in terms of cumulative area and binned grayscale values. The graphical analysis method of Roseen (2002) guided by manual inspection of image pixel values, was used to define the plume area ($\sim$115 m^2). (d) The plume size-spring discharge relationship from the three gauged springs of the lagoon is used to define spring instantaneous discharge based on plume area defined in (c). Panels a, b, c, and d in this figure correspond with box numbers 1, 1b, 1c, and 3, respectively for supplementary Fig. ~~2~~S1.

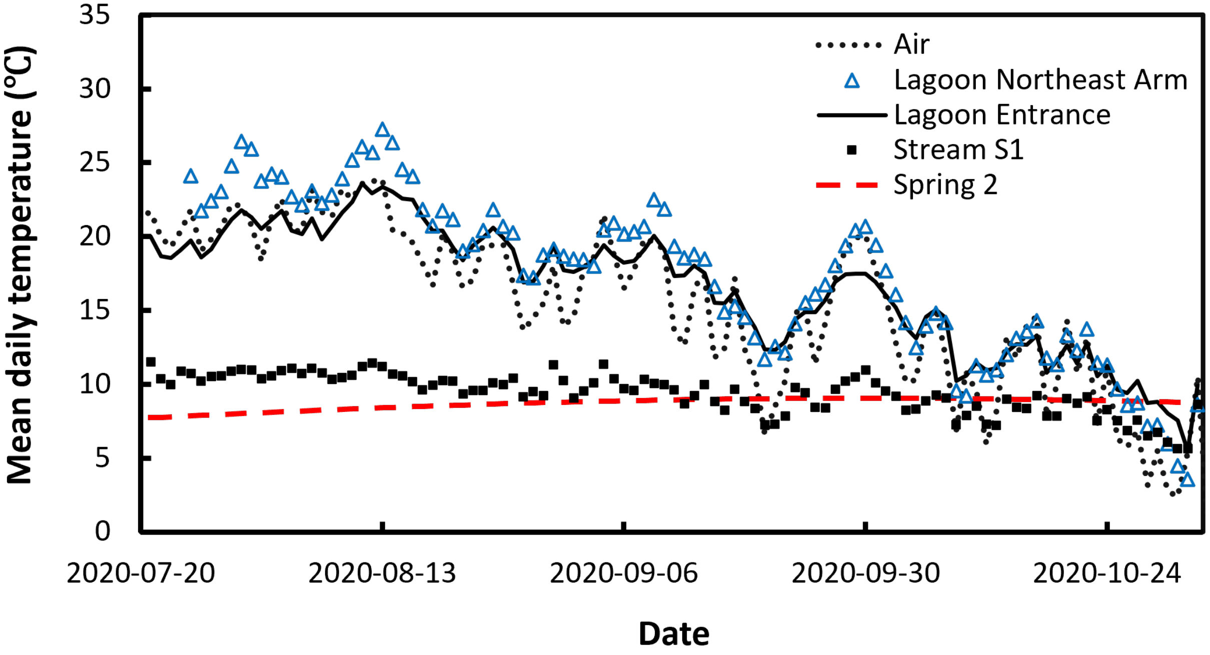

Figure 6: Illustrative examples (subset of monitored locations) of mean daily water temperatures vs. date (yyyyy-mm-dd) for two locations in the Basin Head lagoon (i.e., entrance and northeast arm), Stream S1, and Spring 2 (with tidal effects corrected by considering the temperature only at low tide, see Fig. 7) as well as mean daily air temperature over the final four months of the study period. The lagoon northeast arm water temperature series was calculated from the average of two paired sensors (one at the lagoon water surface and the other at the channel bottom, see Fig. 1). The raw, uncorrected data and inferred annual groundwater temperature signal for Spring 2 is featured in Fig. 7c. Hourly data are in Fig. ~~S8~~S9.

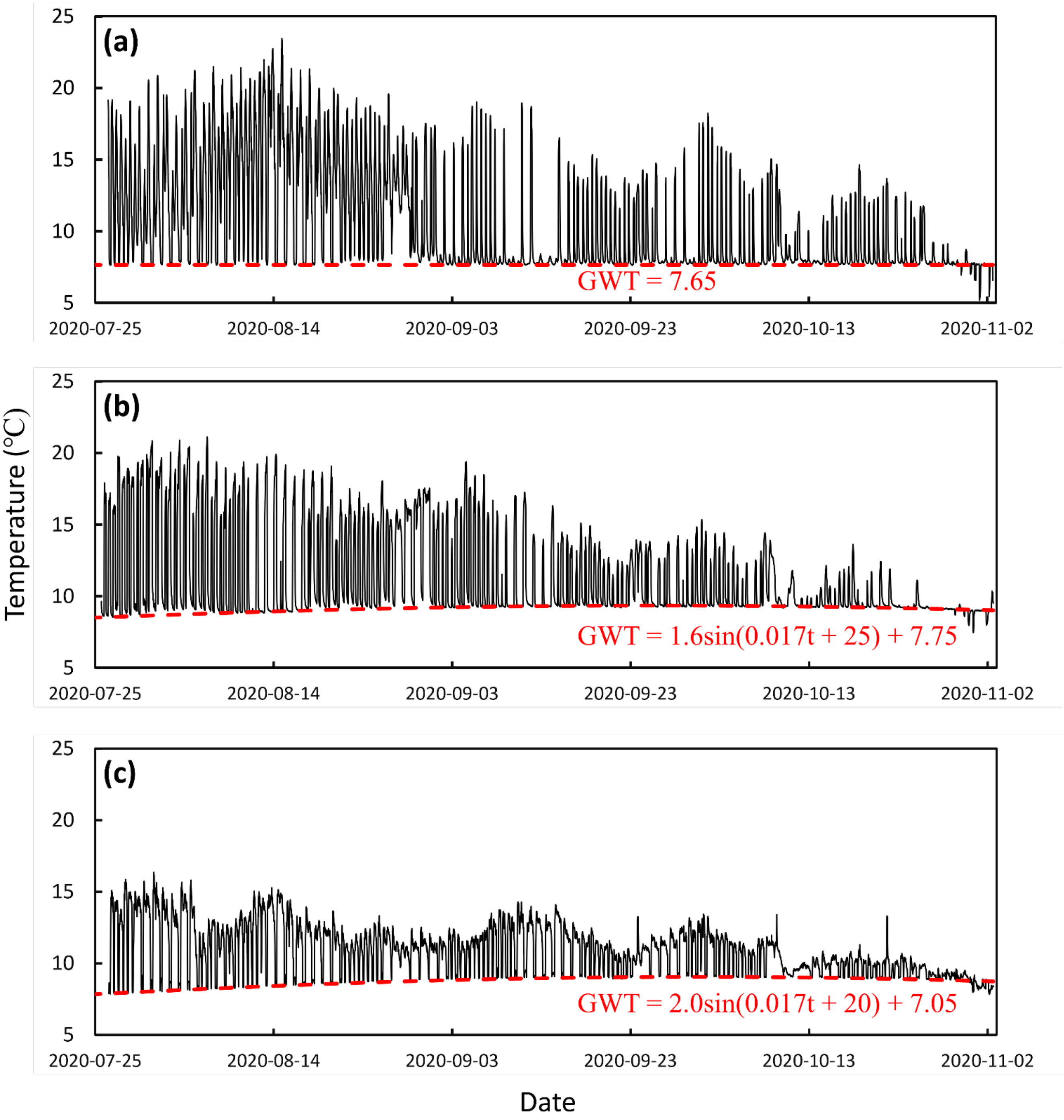

Figure 7: Temperature data (black) from the mouths of (a) Spring 5, (b) Spring 21, and (c) Spring 2 (see Table S2 for locations) vs. date (yyyyy-mm-dd) from ~~the~~ Basin Head lagoon~~ 2020 field investigations~~. The fitted annual temperature sine wave (GWT; in red) has a distinguishable amplitude in Springs 21 and 2 but not in Spring 5. GWT = annual groundwater temperature waveform and t = time in days.

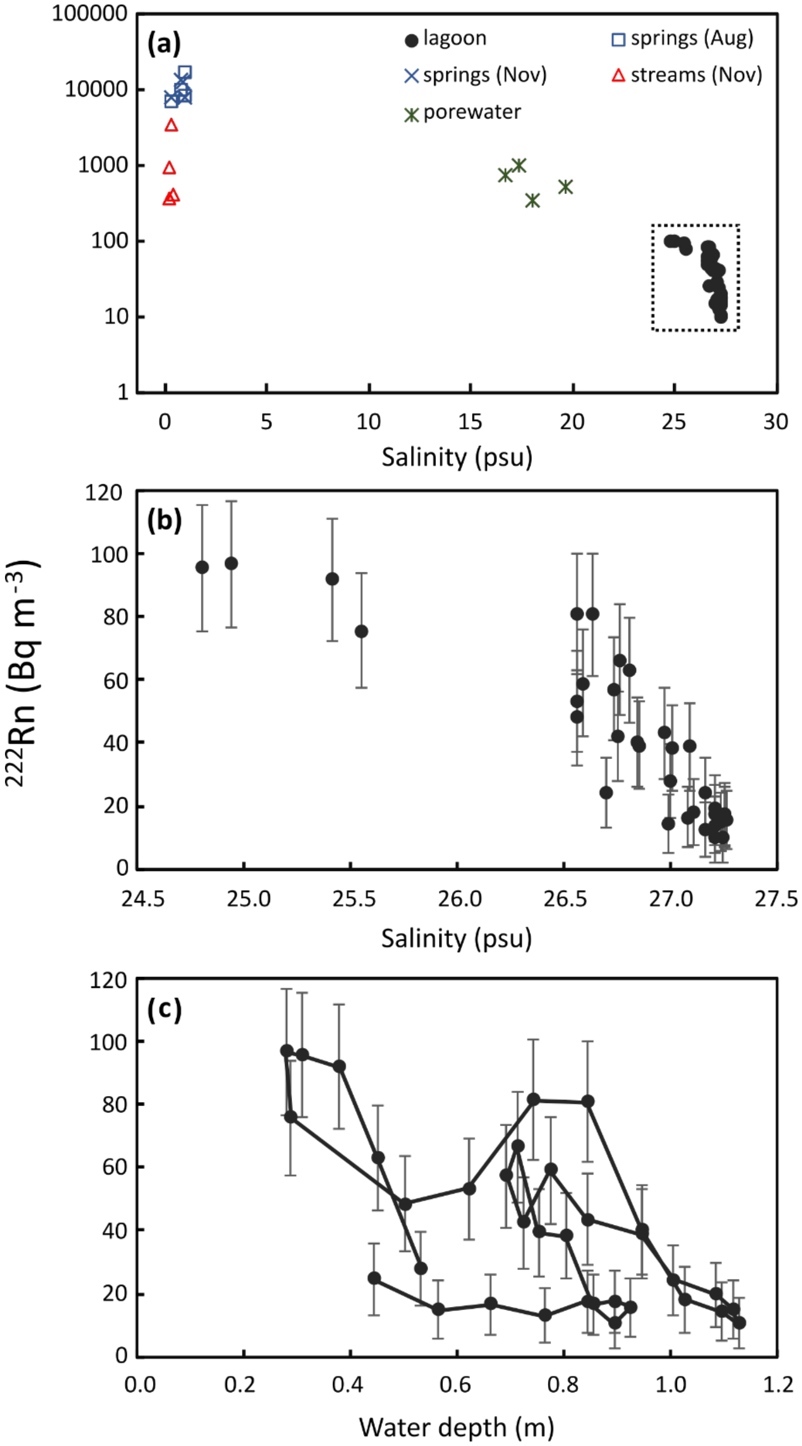

Figure 8: ^{222}**Rn variability versus salinity (a and b) and tidal water level (c), including hysteresis loops over two August 2020 tidal cycles; panel (b) depicts the lagoon data points outlined in (a) at a greater resolution.** ^{222}**Rn values are listed in Table S3.**

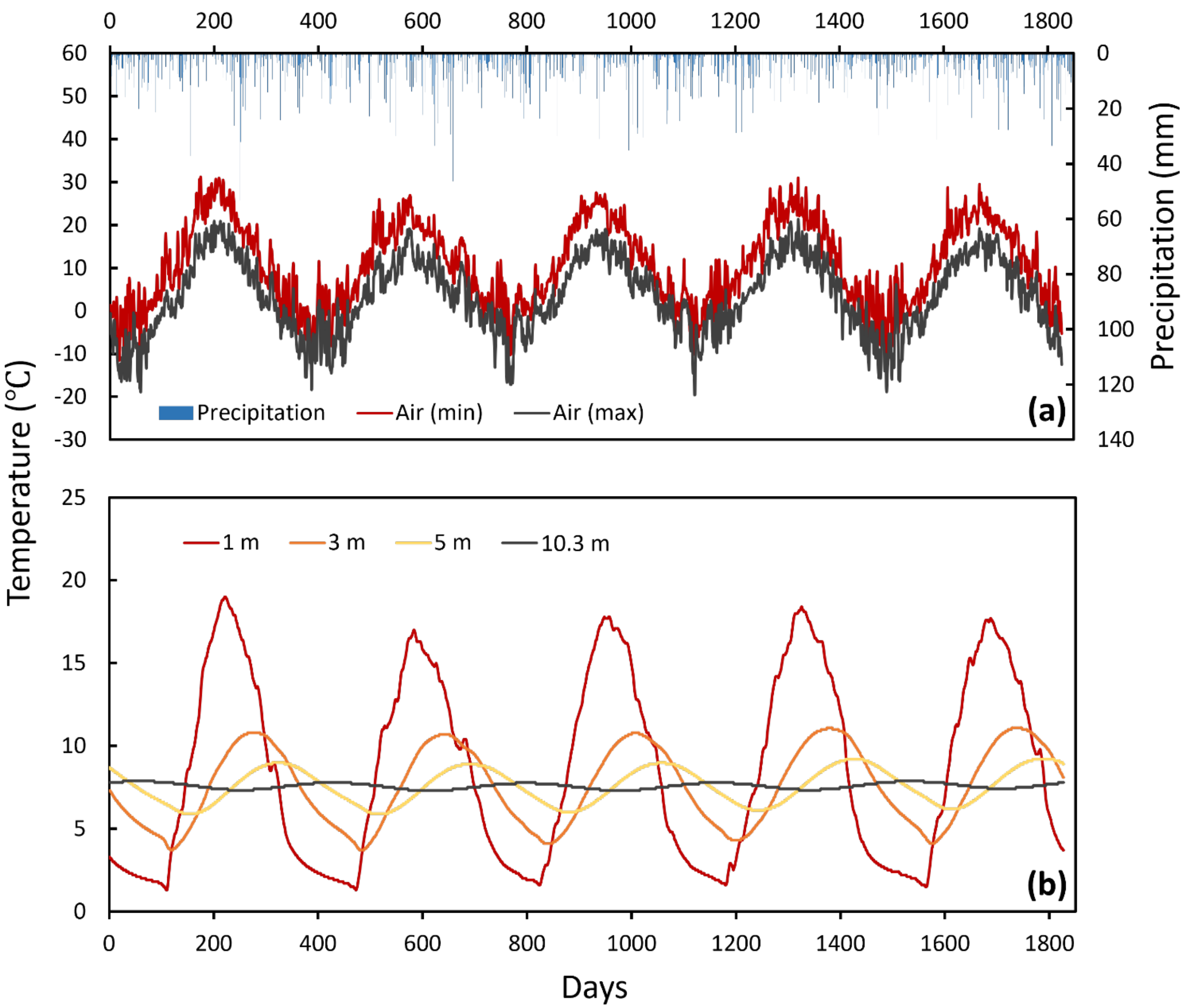
0
200
400
600
800
1000
1200
1400
1600
1800
60
50
40
30
20
10
0
-10
-20
-30
0
20
40
60
80
100
120
140
Precipitation (mm)
Temperature (°C)
Precipitation
Air (min)
Air (max)
(a)
25
20
15
10
5
0
1 m
3 m
5 m
10.3 m
(b)
Days

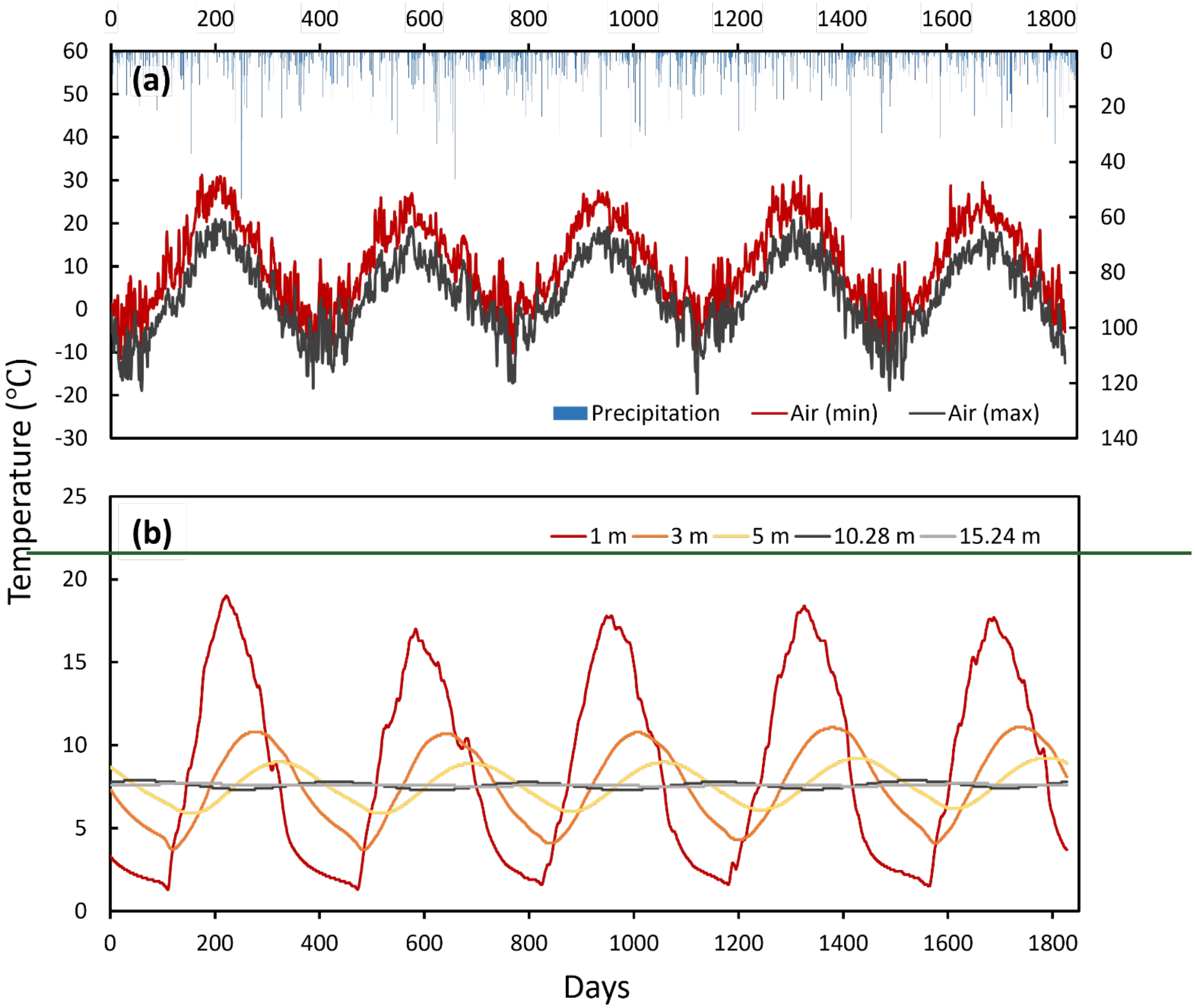

Figure ~~10~~9: Historical simulation data for the years of 2016-2020 extracted from SHAW. (a) Maximum and minimum daily air temperature and total rainfall input to the model. (b) Subsurface temperatures at various depths in response to surface forcing. The temperature data at depths of 1 and 3 m were extracted from the surface domain, whereas the others are from the lower domain. These modelled amplitudes may be compared to measured spring signals to estimate their source depths.

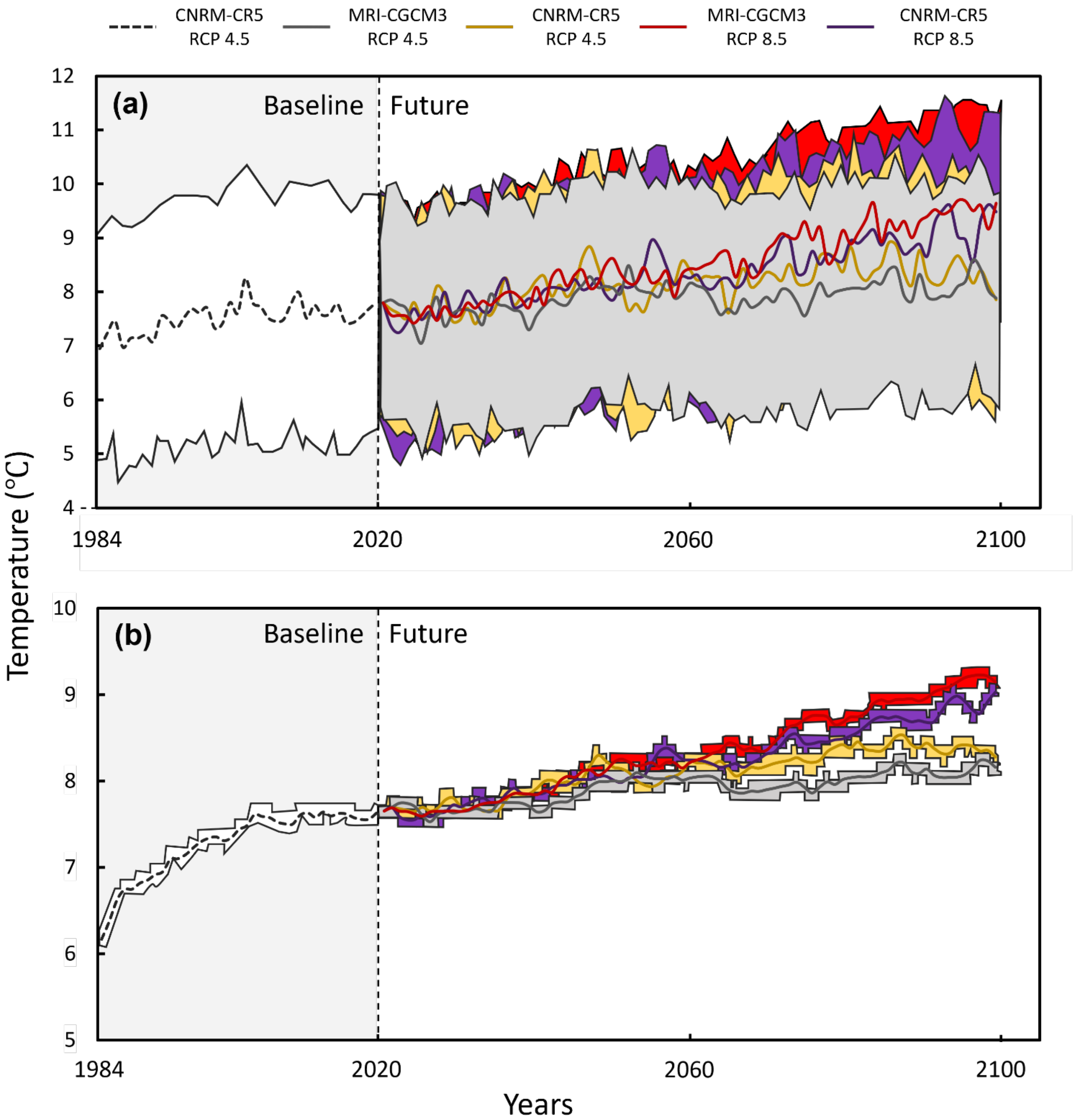

Figure ~~9~~10: Modelled 365-day-averaged subsurface temperatures (lines) and their associated intra-annual range (area) at two depths: (a) 4.2 m and (b) 13.9 m (representing the groundwater temperature sensor depths in our piezometer and the provincial monitoring well, respectively). The historical period (1984-2020) uses the CNRM-CR5 simulation data, and four future simulations were run for the period of 2020-2100. The beginning of the historical simulation involves a period of model domain stabilization.

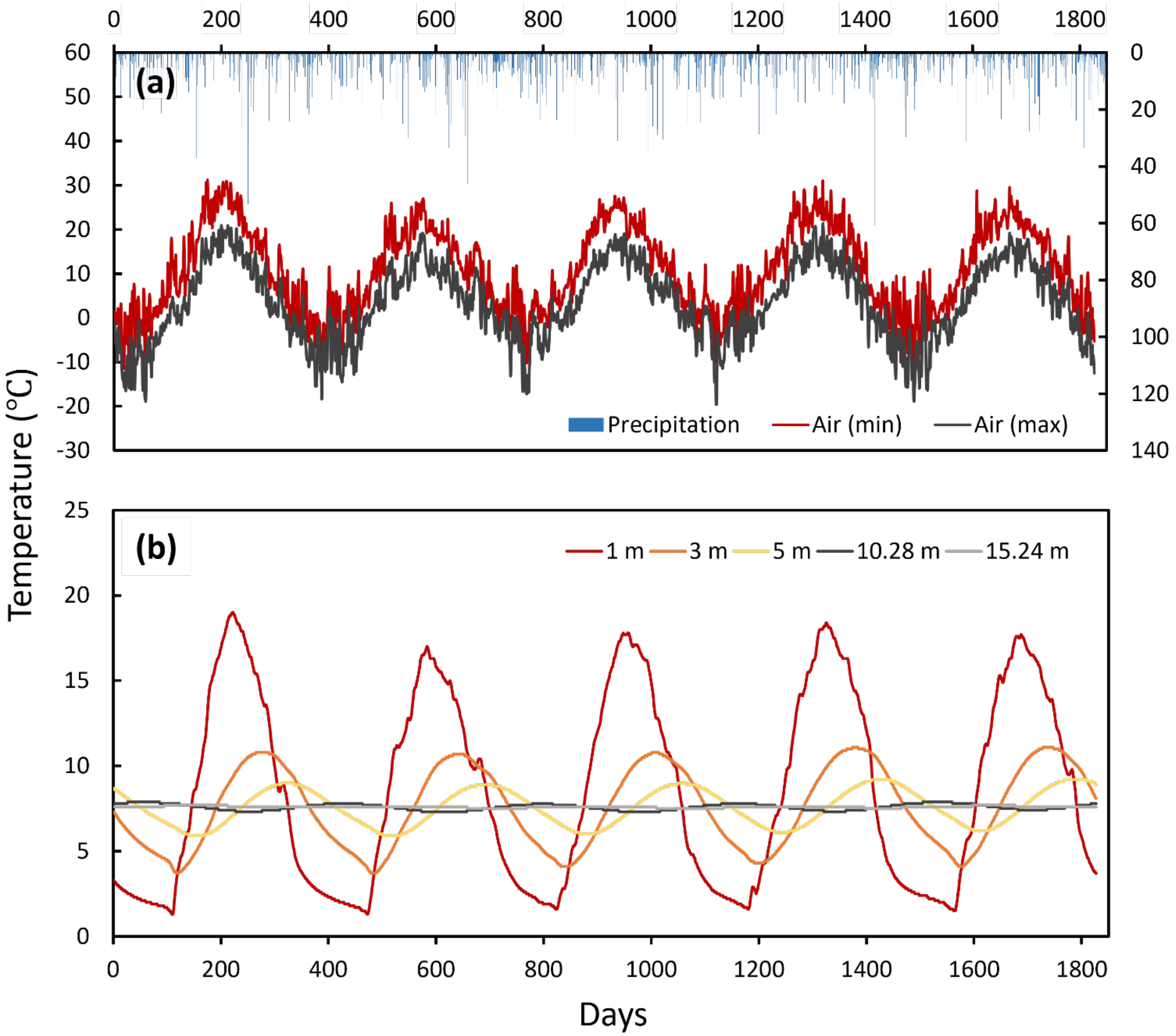

~~Figure 10: Historical simulation data for the years of 2016-2020 extracted from SHAW. (a) Maximum and minimum daily air temperature and total rainfall input to the model. (b) Subsurface temperatures at various depths in response to surface forcing. The temperature data at depths of 1 and 3 m were extracted from the surface domain, whereas the others are from the lower domain. These modelled amplitudes may be compared to measured spring signals to estimate their source depths.~~

Table 1: Basin Head lagoon heat fluxes associated with three advective processes and downwelling shortwave radiation applied across the lagoon surface area. All heat budget components are over the 35-day focused study period. Positive values indicate an addition of sensible energy to the lagoon, while negative values indicate a cooling effect. Lagoon water temperature was approximated as its median value (22°C) to calculate the advective terms (Eq. 1).

Heat budget component	**35-day net heat contribution**	**35-day net water volume (m^3)**	**Approx. mean water temperature (°C)**
Springs	-7.60×10^{12} J (-2.51×10^{6} W)	142,000	8
Streams	-7.67×10^{12} J (-2.53×10^{6} W)	153,000	10
Rainfall	-2.76×10^{11} J (-8.83×10^{4} W)	22,000	19
Downward shortwave radiation	3.89×10^{14} J (1.29×10^{8} W)	NA	NA

Table 2: Simulated groundwater temperatures for the future SHAW simulations at the two studied depths (4.2 m = piezometer sensor depth, while 13.9 m = depth from provincial monitoring well sensor, see text). GCM = Global Circulation Model; RCP = Representative Concentration Pathway.

GCM	**RCP**	**Depth (m)**	**Average annual temperatures (°C)**	**Projected change (range) (°C)[a]**
CNRM-CR5	Historic	4.2	7.45 – 7.80	NA
CNRM-CR5	4.5	4.2	7.88 – 8.45	0.08 – 1.00
CNRM-CR5	8.5	4.2	8.59 – 9.62	0.79 – 2.17
MRI-CGCM3	4.5	4.2	7.90 – 8.61	0.10 – 1.16
MRI-CGCM3	8.5	4.2	9.13 – 9.68	1.33 – 2.23
CNRM-CR5	Historic	13.9	7.61 – 7.63	NA
CNRM-CR5	4.5	13.9	8.26 – 8.41	0.63 – 0.80
CNRM-CR5	8.5	13.9	8.79 – 9.03	1.16 – 1.42
MRI-CGCM3	4.5	13.9	8.08 – 8.25	0.45 – 0.64
MRI-CGCM3	8.5	13.9	9.14 – 9.23	1.51 – 1.62

[a] *The projected temperature change was calculated by comparing the last five years of the future simulation to the last five years of the historic simulation.*

Online Supplemental Material

Article title: ~~*Intertidal spring discharge to a coastal ecosystem and the impacts of climate change on future groundwater temperature: A multi-method investigation*~~ *Present and future thermal regimes of intertidal groundwater springs in a threatened coastal ecosystem*

Journal name: *Hydrology and Earth System Sciences*

Authors: Jason J. KarisAllen[1], Aaron A. Mohammed[1,2], Joseph J. Tamborski[3], Rob C. Jamieson[1], Serban Danielescu[4], Barret L. Kurylyk[1]

[1]Department of Civil and Resource Engineering and Centre for Water Resources Studies, Dalhousie University, Halifax, B3H 4R2, Canada
[2]Department of Earth and Planetary Sciences, McGill University, Montréal, H3A 0E8, Canada
[3]Department of Ocean and Earth Sciences, Old Dominion University, Norfolk, VA, 23529, USA
[4]Water Science and Technology Directorate, Environment and Climate Change Canada, Burlington, ON L7S 1A1, Canada
[5]Agriculture and Agri-Food Canada, Fredericton Research and Development Centre, Fredericton, New Brunswick E3B 4Z7, Canada

Summary of image analysis (box 1, Figure 2 and Figure 5, main text): Rather than developing a per-pixel corrections matrix for the sensor to correct for distortion towards the image periphery, only the central portion of each image was analysed. This study applied FLIR Tools®, ImageJ, and MATLAB® to post-process grayscale intensity data from the thermal infrared images using the procedure summarized in Fig. S1. These products enabled the analysis of high-resolution thermal data and polygonal cropping procedures. Grayscale intensity data was extracted from the thermal images of the spring-sourced plumes and graphed with respect to cumulative area to yield a characteristic S-shape type-curve (Fig. S1). Each 'inflection point' of the graph was used to define 'thermal groups' and the sharp transition zones between them

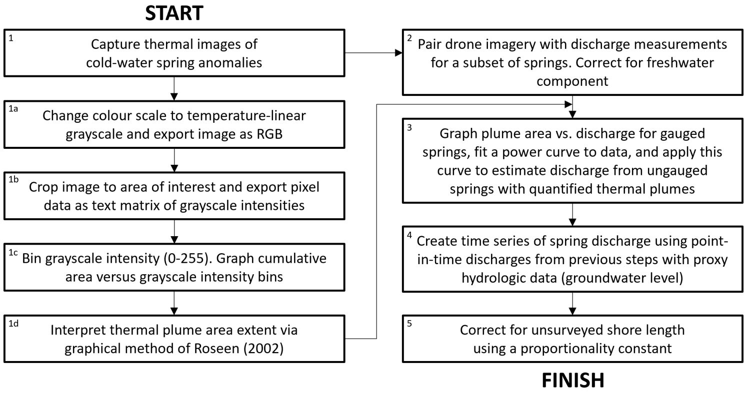

Figure S1: Summary workflow of the spring discharge assessment technique applied in Basin Head lagoon using thermal imagery. Panels a, b, c, and d of Fig. 5 correspond with box numbers 1, 1b, 1c, and 3, respectively

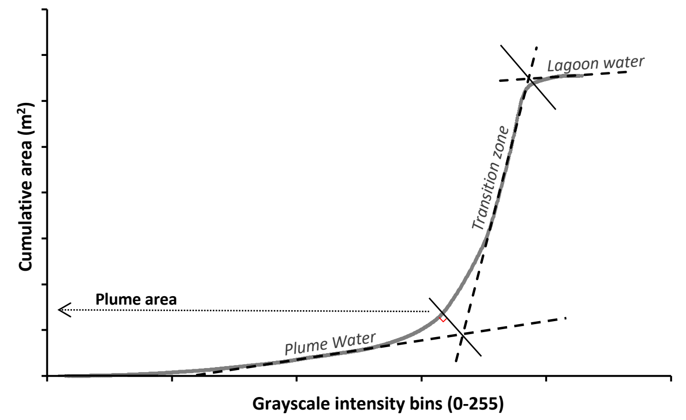

Commented [BK1]: Just moved up from below

Figure S2. Generic characteristic type-curve used in the areal analysis of a thermal-discharge assessment. Inflection points are identified using near-perpendicular lines connecting the type-curve and the linear intersects. The plume thermal group (i.e., plume area) extends to the plume area inflection point. The lagoon thermal group begins at the second inflection point and extends onward, and there is a steep transition zone between groups. See Roseen (2002) for a description of a similar approach.

Tables begin on the following page.

Table S1: Information on sensors deployed for this study. See figures in the Figure Reference column for locations. The IDs in the Map ID column in this table align with the IDs noted in Figs. S3-S6 in this supplement. All associated data can be found in the dataset described in the Data Availability section at the end of the main paper.

	Parameter(s) Provided	Sensor Make/Model	Number of Sensors	Map ID (prefix and ID#)	Approximate Location(s) by ID# (Long, Lat)	Data Period Provided (Discontinuous and varies per parameter)	Figure Reference(s)
Streams	Water temperature	Onset HOBO MX2203 TidbiTs	4	St1, 2, 3, and 4	1) 62.1243660°W 46.3865830°N 2) 62.1246730°W 46.3862840°N 3) 62.0914720°W 46.3957510°N 4) 62.0889510°W 46.3971560°N	Start: 2020-07-21 11:15 End: 2020-11-02 16:30	1 and 6
	Water flow	HOBO U20-001-04 & SonTek Flow Tracker 2	4	St5, 6, 7, and 8	5) 62.1273340°W 46.3867770°N 6) 62.1270000°W 46.3900000°N 7) 62.0952870°W 46.3974070°N 8) 62.0906230°W 46.3987880°N	Start: 2020-07-21 13:00 End: 2020-08-31 23:00	1 and S8~~6~~
Springs	Water temperature	Onset HOBO MX2203 TidbiTs	2	Sp2~~1~~ and 21	1) 62.1194598°W 46.3848724°N 2) 62.0998038°W 46.3905342°N	Start: 2020-07-25 17:30 End: 2020-11-02 16:30	1, 6, 7, S3~~2~~, S4~~3~~, and S5~~4~~
	Water temperature	Onset HOBO MX2203 TidbiTs	1	Sp5~~3~~	3) 62.0889360°W 46.3941150°N	Start: 2019-06-26 0:00 End: 2020-11-02 16:30	1, 7, S3~~2~~, S6~~5~~, and S7
Lagoon	Water temperature	Onset HOBO MX2203 TidbiTs	2	L3 and 4	3&4) 62.0879200°W 46.3950140°N	Start: 2019-06-26 2:45 End: 2020-11-02 16:30	1, 6, and S7
	Water temperature	Onset HOBO MX2203 TidbiTs	2	L1 and 2	1&2) 62.0953385°W 46.3910513°N	Start: 2020-07-25 15:30 End: 2020-11-02 16:30	1 and S7
	Water temperature and pressure	Solinst Levelogger 5 LTC	1	L5	5) 62.1106386°W 46.3817063°N	Start: 2020-07-21 12:30 End: 2020-11-02 16:30	1, 6, and S7~~8~~
Piezometer	Water temperature and pressure	Onset HOBO U20-001-01	1	P1	1) 62.1020736°W 46.3900142°N	Start: 2019-08-17 14:45 End: 2020-11-02 16:30	1, S7
Climate Station	Air temperature, radiation, and precipitation	Onset HOBO Micro Station Logger	1	Cl1	1) 62.1030470°W 46.3890710°N	Start: 2019-06-26 0:00 End: 2020-11-02 16:30	1, 6, and S7

Table S2: Measured thermal plume areas of 34 springs in Basin Head lagoon over the study period (locations displayed in Figure 1b and Figures S3~~2~~-S6~~5~~). The instantaneous discharge of Springs A, B, and C (grey rows) were measured and used to develop the plume size-spring discharge relationship, whereas Springs 1-31 were estimated using their measured area and the developed relationship. The date/time indicates when the thermal image was captured. Area was obtained as indicated in Figures S1~~2~~ and S2~~Figure S1~~ and included short distances of overland flow.

Spring ID	Date/time	Area (m^2)	Discharge ($m^3 s^{-1}$)	Spring location (Lat; Long)
A	22-07-2020 19:37	360	3.1E-03*	46.389305; -62.102322
B	22-07-2020 19:35	51	5.2E-04*	46.390244; -62.10096
C	22-07-2020 19:36	10	7.5E-05*	46.388714; -62.103432
1	29-08-2020 15:27	694	6.2E-03	46.386246; -62.110306
2	29-08-2020 15:33	360	3.1E-03	46.38493; -62.119438
3	24-07-2020 19:33	289	2.5E-03	46.390179; -62.101189
4	22-07-2020 19:36	259	2.2E-03	46.396149; -62.08857
5	21-07-2020 20:17	171	1.4E-03	46.394167; -62.088889
6	24-07-2020 18:16	164	1.4E-03	46.386944; -62.115067
7	24-07-2020 18:16	133	1.1E-03	46.386944; -62.115067
8	24-07-2020 19:29	115	9.6E-04	46.39827; -62.080589
9	22-07-2020 19:36	65	5.3E-04	46.390114; -62.101421
10	21-07-2020 20:15	59	4.8E-04	46.392818; -62.090939
11	24-07-2020 19:29	57	4.6E-04	46.398132; -62.080959
12	22-07-2020 17:04	55	4.4E-04	46.386448; -62.107201
13	24-07-2020 19:30	48	3.9E-04	46.396732; -62.08556
14	22-07-2020 19:37	48	3.9E-04	46.390339; -62.100193
15	24-07-2020 19:36	41	3.3E-04	46.394882; -62.089233
16	24-07-2020 19:31	31	2.5E-04	46.396442; -62.086929
17	24-07-2020 18:13	25	2.0E-04	46.386459; -62.118565
18	21-07-2020 20:15	22	1.8E-04	46.392975; -62.090805
19	24-07-2020 18:18	21	1.6E-04	46.386646; -62.111988
20	24-07-2020 19:36	15.9	1.2E-04	46.394653; -62.088825
21	22-07-2020 19:37	13.3	1.0E-04	46.390591; -62.099422
22	22-07-2020 17:07	12.6	9.7E-05	46.386269; -62.110722
23	21-07-2020 20:16	11.2	8.6E-05	46.393421; -62.089939
24	24-07-2020 19:31	9.2	7.0E-05	46.396744; -62.085999
25	24-07-2020 18:15	7.4	5.6E-05	46.38686; -62.116539
26	24-07-2020 18:14	6.7	5.1E-05	46.386528; -62.118763
27	21-07-2020 20:16	3.1	2.3E-05	46.393661; -62.089458
28	24-07-2020 18:13	2.4	1.7E-05	46.386433; -62.11874
29	21-07-2020 20:16	2.0	1.4E-05	46.393745; -62.089233
30	24-07-2020 19:37	1.9	1.4E-05	46.393871; -62.089138
31	21-07-2020 20:14	1.7	1.2E-05	46.392387; -62.092205

*Measured spring discharges used in the plume size-spring discharge relationship. The accuracy of measured discharges was estimated to be within ±25%.

Table S3: Summary of groundwater springs, baseflow-fed streams and shallow porewaters collected in August and November 2020. Porewater values in parentheses indicate sample collection depth. Stream locations are shown in Figure 1.

Sample ID	Sample Type	Temperature (°C)	Salinity (psu)	^{222}Rn (Bq m^{-3})
August 2020				
Spring A	fractured sandstone spring	8.6	0.93	8,360 ± 1,280
Spring B(1)	fractured sandstone spring	9.8	0.76	10,080 ± 1,670
Spring B(2)	fractured sandstone spring	9.4	0.87	16,570 ± 1,180
Spring C	fractured sandstone spring	11.6	0.25	6,740 ± 880
November 2020				
Spring A	fractured sandstone spring	7.9	0.87	7,530 ± 1,060
Spring B(1)	fractured sandstone spring	9.5	0.71	13,220 ± 470
Spring B(2)	fractured sandstone spring	9.2	0.80	12,620 ± 680
Spring C	fractured sandstone spring	9.3	0.21	7,880 ± 770
Stream S1	Stream	5.3	0.25	3,410 ± 590
Stream S2	Stream	5.0	0.30	410 ± 100
Stream S3	Stream	6.2	0.15	360 ± 110
Stream S4	Stream	6.1	0.15	360 ± 60
Stream S6	Stream	6.2	0.13	940 ± 140
WT1	Porewater (0.2 m)	0.7	16.6	710 ± 300
WT2	Porewater (0.4 m)	0.7	17.3	1,000 ± 410
OP1	Porewater (0.2 m)	7.9	19.6	500 ± 240
MP2	Porewater (0.4 m)	1.6	18.0	340 ± 140

Table S4: Summary of parameters and fluxes used in the ^{222}Rn mass balance.

Term	Definition	Value	Uncertainty	Units
A	Lagoon area	5.90E+05	5.90E+04	m^2
I	Mean excess ^{222}Rn inventory	18	15	Bq m^{-2}
Q_{stream}	Stream discharge	0.05	0.02	m^3 s^{-1}
C_{stream}	Stream ^{222}Rn	1100	1200	Bq m^{-3}
C_{GW}	Fractured-sandstone spring ^{222}Rn	10400	3700	Bq m^{-3}
C_{Ra}	^{226}Ra activity	10	8	Bq m^{-3}
λ_{Rn}	^{222}Rn decay constant	0.181	-	d^{-1}
^{222}Rn Sinks				
J_{atm}	Atmospheric evasion	6.4E+06	6.6E+06	Bq d^{-1}
J_{mix}	Mixing losses	8.4E+07	5.9E+07	Bq d^{-1}
J_{decay}	Radioactive decay	1.9E+06	1.6E+06	Bq d^{-1}
^{222}Rn Sources				
J_{diff}	Molecular diffusion	6.4E+06	3.2E+06	Bq d^{-1}
$J_{Ra\text{-}226}$	^{226}Ra production	1.1E+06	8.5E+05	Bq d^{-1}
J_{stream}	Stream ^{222}Rn flux (inc. baseflow)	4.7E+06	5.6E+06	Bq d^{-1}
J_{spring}	Groundwater ^{222}Rn	8.0E+07	6.0E+07	Bq d^{-1}
-	Groundwater discharge	0.09	0.07	m^3 s^{-1}

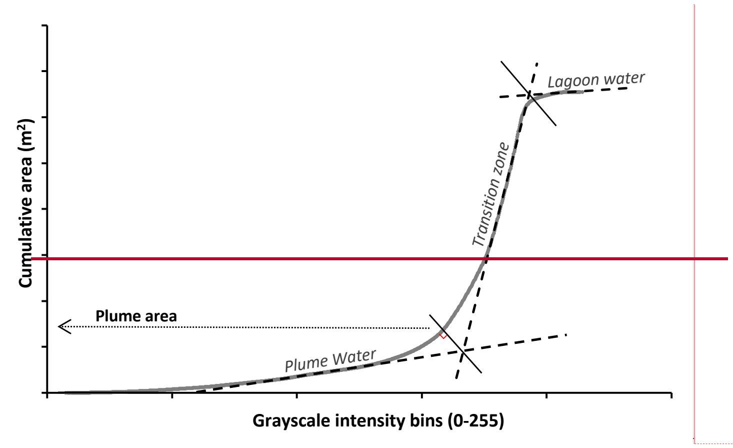

Commented [BK2]: Moved up

~~**Figure S1. Generic characteristic type-curve used in the areal analysis of a thermal-discharge assessment. Inflection points are identified using near-perpendicular lines connecting the type-curve and the linear intersects. The plume thermal group (i.e., plume area) extends to the plume area inflection point. The lagoon thermal group begins at the second inflection point and extends onward, and there is a steep transition zone between groups. See Roseen (2002) for a description of a similar approach.**~~

Table S5. Coarse calibration targets based on field data (transducer measuring groundwater temperature in coastal piezometer, see Figure 1, main text) compared with SHAW modelled results covering this sampling period.

Data ID	**Depth (m)**	**Temperature (°C)**	**Amplitude (°C)**	**Lag (days)**
Coastal piezometer	4.24	5.10 - 9.50[1]	1.80 – 2.20[1]	70 – 100
SHAW Simulation	4.20	7.45 – 7.80[2]	2.10 – 2.20[2,3]	92 – 105

[1] Range of groundwater temperatures measured from 15-minute resolution temperature data gathered discontinuously over a period of two years (2019-2020) from a coastal piezometer (see Figure 1) adjacent to the Basin Head lagoon.

[2] Range of average annual temperature output from the SHAW simulation between 2016 to 2020.

[3] To assess our model output, we also used a provincial monitoring well located nearby the Basin Head watershed that had a sensor at a depth of 13.9 m. Our modeled temperature amplitude at this point was close to the measured amplitude, but off by 0.1°C.

A high-level sensitivity analysis was conducted on model parameters and design elements that were highly uncertain and expected to affect the calibration targets (i.e., subsurface temperature patterns). This assessment focused on the calibration performance and, by extension, the thermal control of the model. The estimated likely range of each of the model parameters/elements listed in Table S6 were tested one at a time. To reflect the high degree of uncertainty involved in this modelling process, only relative qualitative indicators of sensitivity were used for the tested parameters (i.e., low [L], medium [M], and high [H] sensitivity) based on the magnitude of their influence on calibration performance over their expected range (i.e., how much they changed the subsurface temperatures of the domain). Table S6 presents the resultant uncertainty (binned into three categories) for each parameter.

Table S6. Qualitative, relative attribution of sensitivity to SHAW model input parameters. Letters indicate low (L), medium (M), and high (H) model sensitivity to the respective parameter.

Model Parameter/Element	**Sensitivity**
Residue layer	H
Lower boundary temperature	H
Lower boundary depth	M
Snow/rain threshold	M
Water table depth	M
Shallow organic content	L
Initial domain temperatures	L
Soil compositions	L
Soil porosity	L
Soil density	L

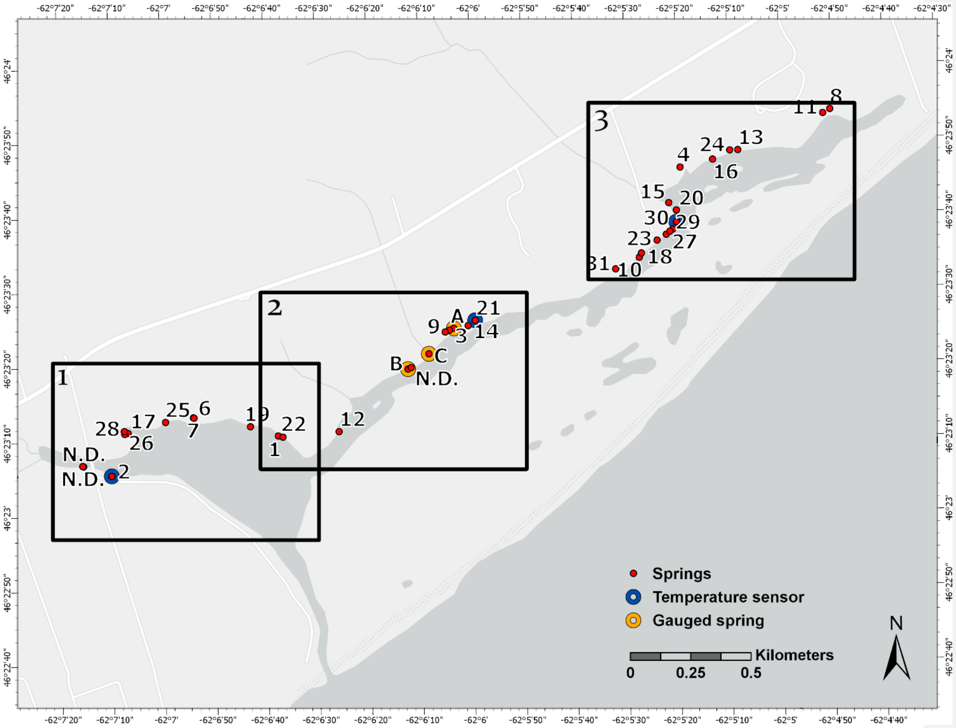

Figure S3~~2~~. (Series image 1 of 4) Spring locations in the Basin Head lagoon. Black boxes each represent an area depicted in subsequent series images that include spring IDs with reference to Table S1. (1) Figure S~~Figure S~~4, (2) Figure S~~Figure S~~5, and (3) Figure S~~Figure S~~6. Basemap is attributed to Esri, HERE, Garmin, FAO, NOAA, USGS, © OpenStreetMap contributors, and the GIS User Community.

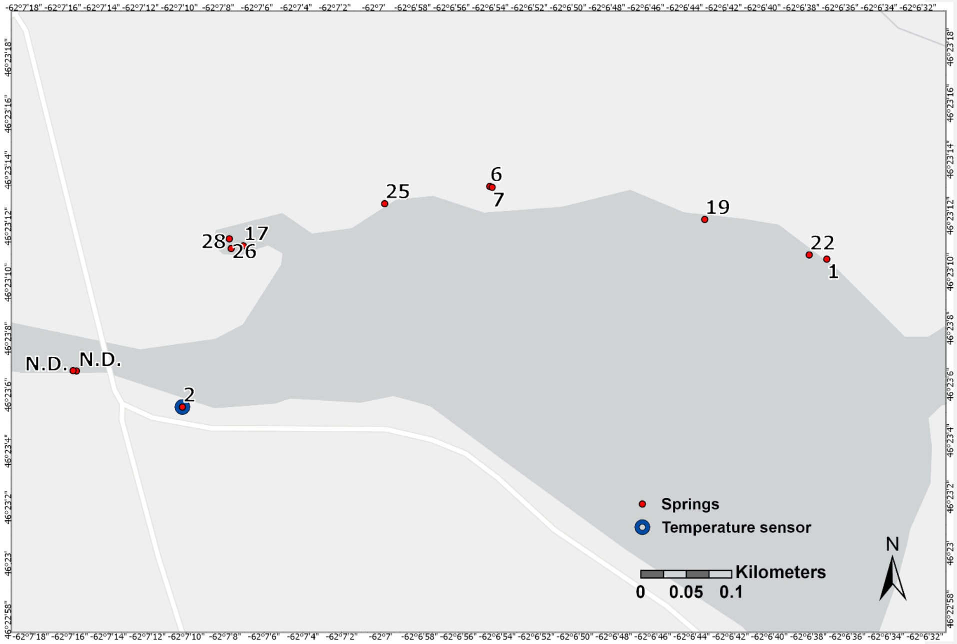

Figure S~~3~~4~~.~~ (Series image 2 of 4) Locations and IDs of springs in main basin of the Basin Head lagoon. N.D. = No Data. Basemap is attributed to Esri, HERE, Garmin, FAO, NOAA, USGS, © OpenStreetMap contributors, and the GIS User Community.

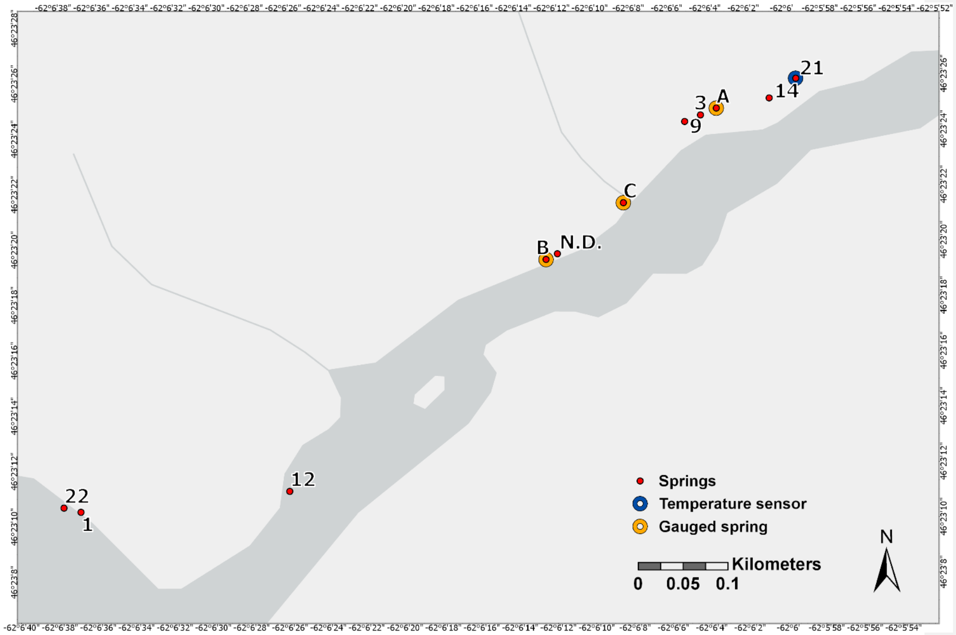

Figure S5~~4.~~ (Series image 3 of 4) Locations and IDs of springs in the main basin and north-east arm of the Basin Head lagoon. N.D. = No Data. Map prepared in ArcGIS Pro (Version 2.3.3, 2018). Basemap is attributed to Esri, HERE, Garmin, FAO, NOAA, USGS, © OpenStreetMap contributors, and the GIS User Community.

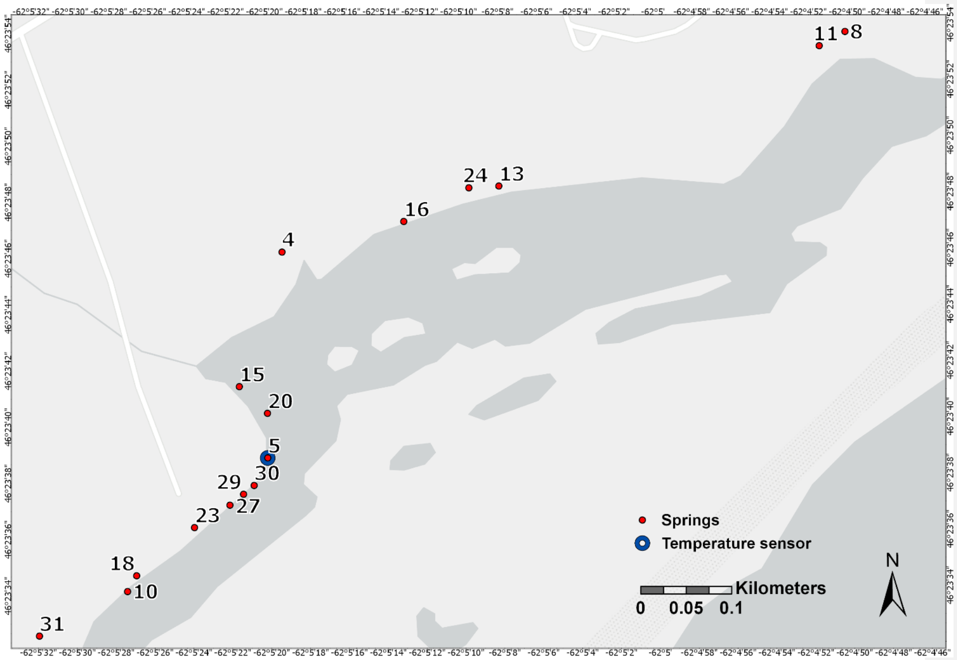

Figure S6~~5~~. (Series image 4 of 4) Locations and IDs of springs in the upper north-east arm of the Basin Head lagoon. Basemap is attributed to Esri, HERE, Garmin, FAO, NOAA, USGS, © OpenStreetMap contributors, and the GIS User Community.

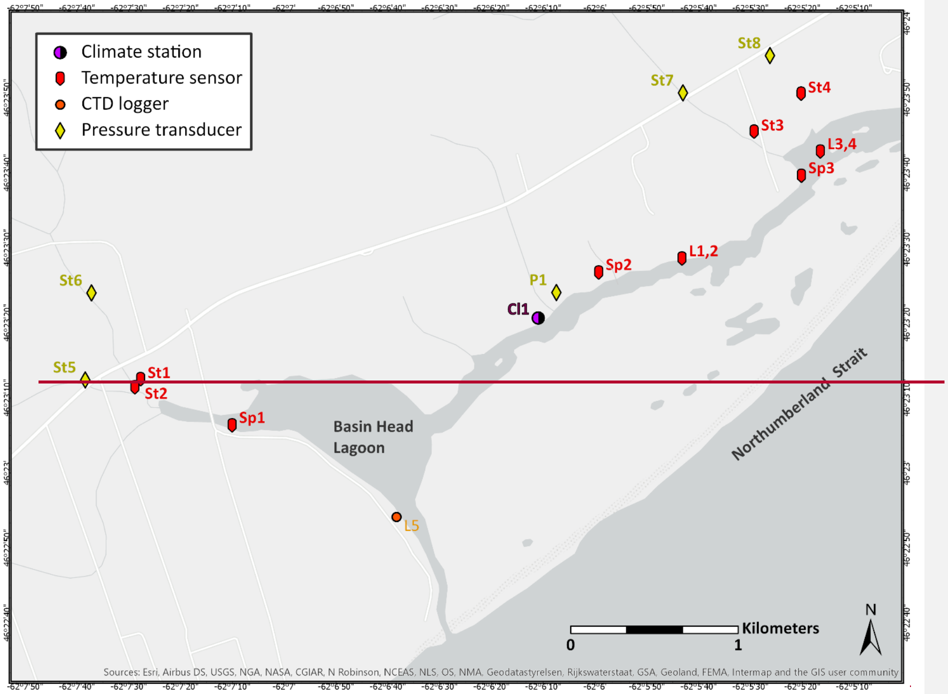

Sources: Esri, Airbus DS, USGS, NGA, NASA, CGIAR, N Robinson, NCEAS, NLS, OS, NMA, Geodatastyrelsen, Rijkswaterstaat, GSA, Geoland, FEMA, Intermap and the GIS user community

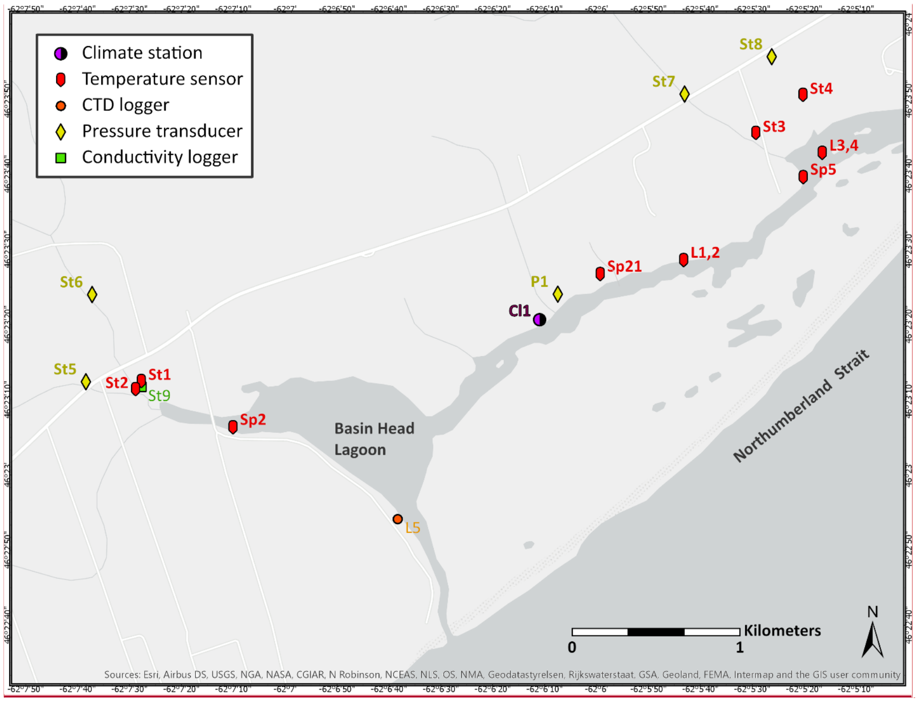

Sources: Esri, Airbus DS, USGS, NGA, NASA, CGIAR, N Robinson, NCEAS, NLS, OS, NMA, Geodatastyrelsen, Rijkswaterstaat, GSA, Geoland, FEMA, Intermap and the GIS user community

Figure S7~~6~~: A map of all sensors with data include in the data archive (see Data Availability section of main paper). This additional map is included to provide context for the Sensor IDs noted in Table S1, which correspond to the sensor IDs in the figure. To enable the clear presentation of the sensor IDs, no springs are shown in this figure. Basemap is attributed to Esri, HERE, Garmin, FAO, NOAA, USGS, © OpenStreetMap contributors, and the GIS User Community.

Commented [BK3]: Numbering updated on three springs to ensure consistency across all figures and tables

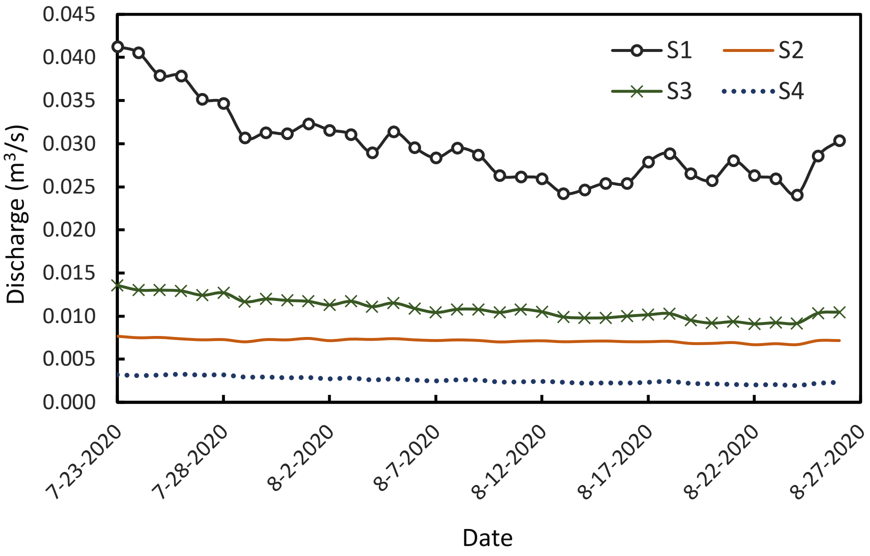

Figure S8~~7~~: Daily stream hydrographs of the primary four tributaries discharging to Basin Head lagoon over the 35-day focussed study period (date presented as yyyy-mm-dd). Discharge is entirely attributed to baseflow over this period. See Figs. 1 or S7 for locations.

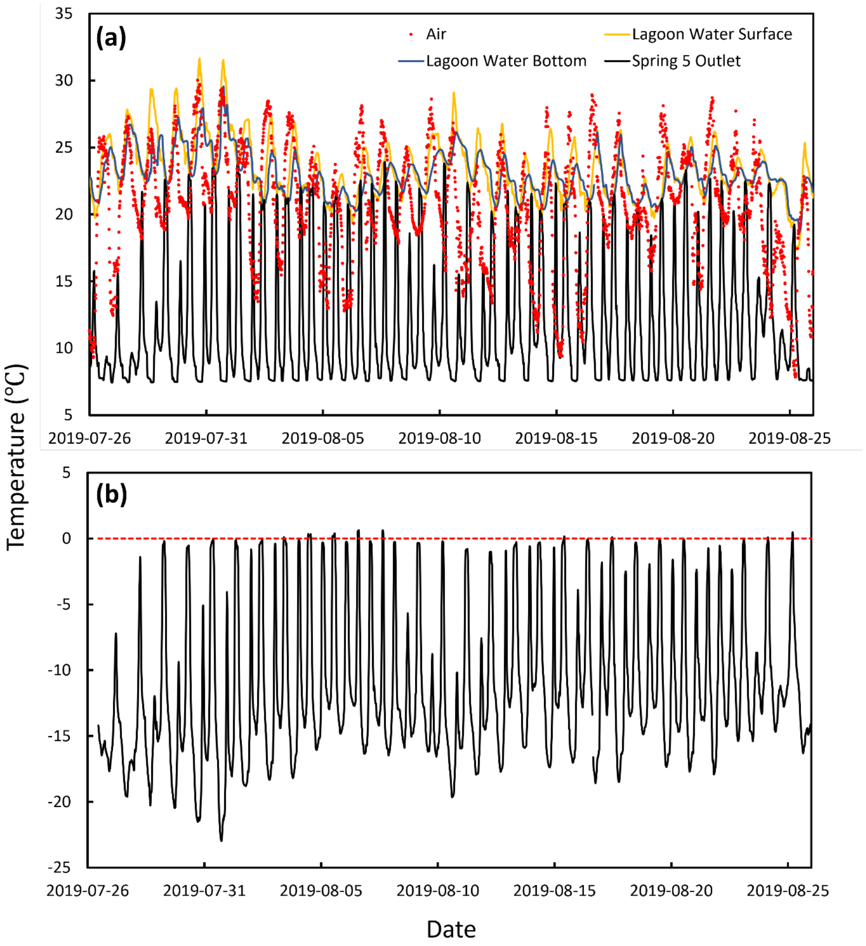

Figure S98: (a) Hourly local air temperature and water temperature data (top and bottom of water column, sensors L3 and L4, respectively) from the upper north-east arm of Basin Head lagoon (date presented as yyyy-mm-dd). (b) The difference between Spring 5 temperature and the average of the channel surface and bottom temperature (shown in a) approximately 30 m away. This difference demonstrates the local cooling effect of springs on the lagoon water temperature and can be inserted into Eq. (1) in the main text.